SIMULATION OF MULTISCALE HYDROPHOBIC LIPID DYNAMICS VIA EFFICIENT INTEGRAL EQUATION METHODS*

SZU-PEI P. FU † , ROLF J. RYHAM † , ANDREAS KLÖCKNER ‡ , MATT WALA ‡ , SHIDONG JIANG § , AND Y.-N. YOUNG §

Abstract. In this paper a mathematical model for long-range, hydrophobic attraction between amphiphilic particles is developed to quantify the macroscopic assembly and mechanics of a lipid bilayer membrane in solvents. The non-local interactions between amphiphilic particles are obtained from the first domain variation of a hydrophobicity functional, giving rise to forces and torques (between particles) that dictate the motion of both particles and the surrounding solvent. The functional minimizer (that accounts for hydrophobicity at molecular-aqueous interfaces) is a solution to a boundary value problem of the screened Laplace equation. We reformulate the boundary value problem as a second-kind integral equation (SKIE), discretize the SKIE using a Nyström discretization and 'Quadrature by Expansion' (QBX) and solve the resulting linear system iteratively using GMRES. We evaluate the required layer potentials using the 'GIGAQBX' fast algorithm, a variant of the Fast Multipole Method (FMM), yielding the required particle interactions with asymptotically optimal cost. Solving a mobility problem in Stokes flow is incorporated to obtain corresponding rigid body motion. The simulated fluid-particle systems exhibit a variety of multiscale behaviors over both time and length: Over short time scales, the numerical results show self-assembly for model lipid particles. For large system simulations, the particles form realistic configurations like micelles and bilayers. Over long time scales, the bilayer shapes emerging from the simulation appear to minimize a form of bending energy.

Key words. Energy Variation, Integral Equation Method, Lipid Dynamics

AMS subject classifications. 31A10, 35A15, 92C05

2

3

4

5

6

9

10

11

12 13

14

15

17 18

19

20

21

22

23

24

25

26

27 28

29

30

31

32 33

34

35

36

37

38

39

40

41

42

1. Introduction. In recent years, researchers have developed various macroscopic continuum formulations and a number of numerical methods for calculating energy minimizing and time-dependent shapes of lipid bilayer membranes, vesicles and red blood cells. While the Helfrich free energy of a lipid bilayer membrane assumes an infinitely thin membrane thickness [74, 33], many other continuum models incorporate more lipid physics [2, 6, 61] and membrane structures [12, 13, 21, 28, 43]. These refined continuum formulations are in principle capable of capturing topological changes of a lipid bilayer membrane, such as membrane fusion and fission. However, no simulations of membrane fusion or fission based on these refined formulations are available in the literature (to our knowledge), possibly due to the numerical challenges to efficiently and accurately resolve structures on the scale of membrane thickness.

Changes in topology of bilayer membranes, as occur in bilayer membrane fusion, pore formation and protein insertion, for example, involve the introduction of a hydrophobic fissure in the normally intact monolayer surface. Due to the relatively large tension of a hydrocarbon-water interface, the energy of a hydrophobic fissure can dominate the membrane's elastic energy, making it necessary to also take into account local interactions at the molecular level [22, 14]. Moreover, in many subcellular structures, membrane energies are dominant in high curvature regions only a few lipids wide [34, 82].

^{*} Submitted to the editors DATE.

[†]Department of Mathematics, Fordham University, Bronx, NY 10458 (sfu17@fordham.edu, rry-ham@fordham.edu)

[‡]Department of Computer Science, University of Illinois at Urbana-Champaign, Urbana, IL 61801 (andreask@illinois.edu, wala1@illinois.edu).

[§]Department of Mathematical Sciences, New Jersey Institute of Technology, Newark, NJ 07102 (shidong.jiang@njit.edu , yyoung@njit.edu).

Based on these observations, we focus on topological changes with mesoscopic interactions in a semi-continuum framework where the lipids are coarse-grained into amphiphilic Janus-type particles while their interactions with each other and the solvents are described at a continuum level. This hybrid approach provides a bridge from microscopic molecular formulation to macroscopic continuum description of a lipid bilayer membrane. Furthermore, the continuum limit of our hybrid mesoscopic model may facilitate efficient numerical algorithms for simulating fusion/fission of lipid bilayer membranes of physically relevant membrane size and dynamic duration.

Modern molecular dynamics (MD) simulators (such as MARTINI [52] and LAMMPS [66]) have the advantage in that they resolve all relevant molecular details, and have been widely employed to simulate fully atomistic or coarse-grained lipid bilayer membrane based on pairwise interactions [11, 23, 37, 38, 52, 81]. Traditionally, MD numerical methods use explicit fluid particles such as coarse-grained water molecules and pairwise Lennard-Jones interactions. There is the disadvantage, though, that an enormous number of water molecules and long computation time are needed in MD simulations, and it remains a great challenge to compute the hydrodynamic interactions of the lipid membrane at micron size for durations long enough to make physical predictions. One way to mitigate long computation time is to compute hydrodynamic interactions using an implicit solvent and Stokesian dynamics [4].

In the present work, we propose a novel approach to lipid-lipid interactions called the hydrophobic attraction domain functional (HADF). Let Ω be an open, exterior domain in \mathbb{R}^n representing water surrounding a collection of amphiphilic particles, e.g. lipids. For dispersed particles, the energy associated with hydrophobic interfaces behaves as a surface energy. When nearby, particles decrease their energy by aggregating and sequestering their hydrophobic interfaces from water. These interactions are well-described by the Ginzburg-Landau-type domain functional

69 (1.1)
$$\Phi(\Omega, f) = \gamma \min_{u \in \mathcal{A}} I[u],$$

70 where

71 (1.2)
$$I[u] = \int_{\Omega} \rho |\nabla u|^2 + \rho^{-1} u^2 \, dx.$$

Here $\mathcal{A} = \{u \in W^{1,2}(\Omega) : u = f \text{ on } \Sigma\}$ is the admissible class and f with range [0,1] is the hydrophobicity label for the water-particle interface $\Sigma = \partial \Omega$. The parameter $\gamma > 0$ is interfacial tension. Its value in bilayers has been widely investigated in both numerical and theoretical studies [18, 24, 56, 65]. For a Lipschitz domain Ω and for f the trace of a function in $W^{1,2}(\Omega)$ [19], the existence of a unique minimizer to (1.1) is a straightforward consequence of the closest point theorem [46].

The scalar function u of (1.1) models disruption in the hydrogen bonding network [17, 53]. For a point $x \in \Sigma$ representing a hydrophobic interface, water mobility is restricted and there u(x) = f(x) = 1. Conversely, u(x) = f(x) = 0 at a point $x \in \Sigma$ representing a hydrophilic interface where water mobility is unrestricted. In the water region, u in (1.1) is a solution to the boundary value problem (BVP) of the screened Laplace equation:

84 (1.3)
$$\begin{cases} -\rho^2 \Delta u + u = 0 & \text{in } \Omega, \\ u(x) = f(x) & \text{on } \Sigma, \\ u(x) \to 0, & \text{as } x \to \infty. \end{cases}$$

Solutions u of (1.3) have a boundary layer of thickness $\rho > 0$. Thus disruption in hydrogen bonding modeled by (1.3) extends into the bulk with characteristic distance ρ [15, 54].

The hydrophobic force is the first variation of the functional Φ with respect to the shape of the domain Ω . The challenge in the present work is to compute the hydrophobic force between several bodies of arbitrary shape and configuration. Section 2 carries out the variation for rigid body motions, and this reduces to a set of boundary integrals for the hydrophobic forces and torques. For simulations, we utilize a boundary condition f representing surface portions of lipid tail and lipid head, and we adopt an excluded volume repulsion to avoid particle collisions in the many-body simulations. As an illustration, Figure 1 shows the self-assembly process for three Janus-type particles in a viscous fluid.

An important feature of the model is that the potential Φ and its intermolecular forces and torques, in contrast to that of coarse-grained theories, do not arise from any pairwise potentials (see Appendix A). To leading order, the attraction between particle pairs predicted by (1.1) is in accord with experimental force-distance curves [17, 48, 54]. The functional (1.1), however, requires modification for account for sub-nanometer force oscillations observed in experiment, e.g. through the inclusion of higher order terms. Nevertheless, the HADF captures the essential features of amphiphile self-assembly, and the variational calculations and numerical methods generalize to more complicated domain functionals.

An essential principle for molecular or particle based approaches is to ensure that the total free energy accounting for lipid-lipid and lipid-water interactions gives rise to an equivalent elastic characterization of membranes as determined by experimental measurements [77, 78]. Section 3 examines the elasticity of bilayer particle configurations. We obtain physical quantities such as bending modulus, tilt modulus and stretching modulus by setting up corresponding equilibrium simulations from continuum theory [41, 58, 76].

Section 4 formulates the mobility problem to calculate hydrodynamics from the hydrophobic stress. The dynamics for many-particle simulations yield physically reasonable time scales and configurations. For example, we can track the particle dynamics over the nanosecond range needed for rapid particle self assembly, up to the microseconds range where bilayer and micelle shapes evolve over a slower time scale [69, 70].

Calculating the particle dynamics requires rapid, on-the-fly solution of (1.3). In section 5, we present a new SKIE formulation for the boundary value problem (1.3), derived from a representation of the solution in which the unknowns are only on the boundary Σ . In section 6, we describe an approach to applying a recently developed QBX-FMM scheme for discretizing the SKIE accurately and adaptively, solving the resulting linear system and evaluating the desired physical quantities afterwards accurately and rapidly. The resulting scheme has linear complexity with an optimal number of unknowns for the simulation of particle dynamics at each time step. To compare the computational cost against MD simulations, even solvent free coarse-grained models have at least $O(N^2)$ complexity in the number of particle N [11, 60].

2. Intermolecular Forces and Torques. We calculate the first variation of Φ with respect to rigid body deformations [1, 73]. Consider N-many, rigid particles represented by disjoint, bounded, closed regions P_1, P_2, \ldots, P_N in \mathbb{R}^n , n = 2, 3. The

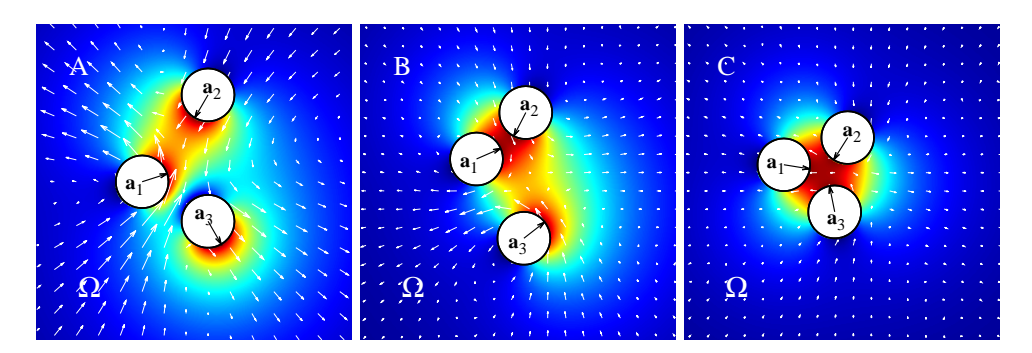


Fig. 1. The figure illustrates hydrophobic attraction of amphiphiles in a zero-Reynolds number fluid. The black arrows are the directors \mathbf{d}_i of the particles centered at \mathbf{a}_i , i=1,2,3. The white arrows are the fluid velocity. The color map has dark blue is for u=0 (lipid heads) and dark red is for the hydrophobic interface u=1 (lipid tails). Activity, shown as pseudo-color shading in the figure, extends from the hydrophobic interface into the bulk. Going from panels A to B, particles \mathbf{a}_1 and \mathbf{a}_2 come together and \mathbf{a}_3 rotates counterclockwise. In panel C, the particles sequester activity to a single hydrophobic core.

water region (the exterior domain) and particle-water interface are

133 (2.1)
$$\Omega = \mathbb{R}^n \setminus \bigcup_{i=1}^N P_i, \quad \Sigma = \bigcup_{i=1}^N \partial P_i,$$

134 respectively. Throughout, ν denotes the unit outward normal to Ω , and ν_i denotes

the unit outward normal to P_i . Note that ν and ν_i have opposite orientation, as

illustrated in Figure 2. Suppose that u is the solution to the screened Laplace BVP

137 (1.3) with the material label f. Then the force \mathbf{F}_i and torque τ_i^0 acting on particle

138 P_i are

139 (2.2)
$$\mathbf{F}_{i} = \int_{\partial P_{i}} \mathbf{T} \cdot \nu_{i} \, dS, \quad \tau_{i}^{0} = \int_{\partial P_{i}} \mathbf{r}_{0} \times (\mathbf{T} \cdot \nu_{i}) \, dS,$$

140 where

141 (2.3)
$$\mathbf{T} = \gamma \rho^{-1} u^2 \mathbf{I} + 2\rho \gamma (\frac{1}{2} |\nabla u|^2 \mathbf{I} - \nabla u \otimes \nabla u),$$

142 is the hydrophobic stress and \mathbf{r}_0 is the position vector relative to the origin $\mathbf{0}$. To

ensure that (2.2) is well-defined and to guarantee differentiability of the domain func-

tional, we that Ω is a $C^{2,\alpha}$ domain and that $f = \tilde{f}$ on Σ for some $\tilde{f} \in C^{2,\alpha}(\overline{\Omega})$.

To compare $\Phi(\Omega, f)$ against that of competing domains, consider a one-parameter family of rigid transformations

147 (2.4)
$$\mathbf{x}_i(\mathbf{X}, \epsilon) = \mathbf{c}_i(\epsilon) + \mathbf{Q}_i(\epsilon)\mathbf{X},$$

parametrized by $\epsilon \in \mathbb{R}$. The vector $\mathbf{c}_i(\epsilon)$ and tensor $\mathbf{Q}_i(\epsilon)$ give the displacement and rotation of the particle P_i , $i=1,\ldots,N$, relative to the origin. They satisfy $\mathbf{c}_i(0)=\mathbf{0}$ and $\mathbf{Q}_i(0)=I$ so that $\mathbf{x}_i(\mathbf{X},0)$ is the identity transformation; $\mathbf{Q}_i(\epsilon)\mathbf{Q}_i^T(\epsilon)=I$ for all ϵ . The distance between P_i and P_j is positive whenever $i\neq j$. Therefore, for ϵ in an open interval about 0, let

153 (2.5)
$$\Omega_{\epsilon} = \mathbb{R}^n \setminus \bigcup_{i=1}^N \mathbf{x}_i(P_i, \epsilon), \quad \Sigma_{\epsilon} = \partial \Omega_{\epsilon}, \quad f_{\epsilon}(\mathbf{x}_i(\mathbf{X}, \epsilon)) = f(\mathbf{X}), \quad \mathbf{X} \in \partial P_i.$$

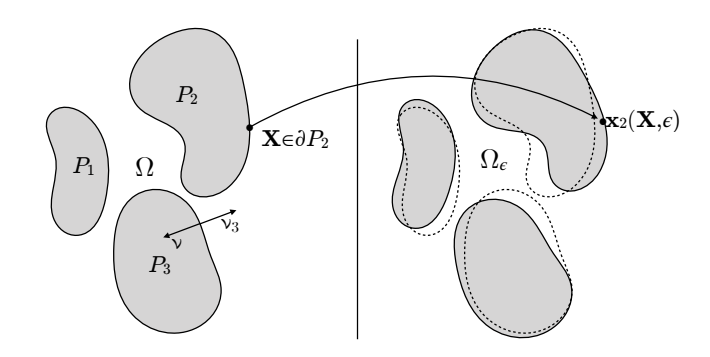


Fig. 2. On the left are three particles P_1 , P_2 and P_3 forming the exterior domain Ω . Rigid transformation of each particle (right panel) leads to the perturbed exterior domain Ω_{ϵ} and changes in the relative positions of the material label f_{ϵ} , resulting in variations in the hydrophobic potential Φ .

- Finally, let $u_{\epsilon}(x)$ be the one-parameter family of solutions to the perturbed boundary
- value problem of screened Laplace equation

156 (2.6)
$$-\rho^2 \Delta u_{\epsilon} + u_{\epsilon} = 0 \text{ in } \Omega_{\epsilon}, \quad u_{\epsilon} = f_{\epsilon} \text{ in } \Sigma_{\epsilon}, \quad u_{\epsilon} \to 0 \text{ as } x \to \infty.$$

- The domain Ω_{ϵ} and boundary Σ_{ϵ} are the water region and water-molecule interface
- after transforming each particle according to its rigid motion (2.4) (see Figure 2). For
- 159 $x \in \Omega$, let

$$\dot{u}(x) = \frac{d}{d\epsilon} u_{\epsilon}(x) \Big|_{\epsilon=0},$$

and extend \dot{u} continuously to $\overline{\Omega}$. Due to (2.5), we have the transport identity

162 (2.7)
$$\dot{u} + \nabla u \cdot \dot{\mathbf{x}} = 0 \text{ on } \Sigma,$$

- where $\dot{\mathbf{x}}(\mathbf{X}) = \frac{d\mathbf{x}_i}{d\epsilon}(\mathbf{X}, 0)$ whenever $\mathbf{X} \in P_i$. (Note, however, that the values of \dot{u} in Ω
- are determined by the BVP (2.6), and therefore do not generally satisfy this transport
- 165 relation.)
- Applying the Reynolds transport theorem [47], we obtain

167 (2.8)
$$\frac{d}{d\epsilon} \Phi(\Omega_{\epsilon}, f_{\epsilon}) \Big|_{\epsilon=0} = \gamma \frac{d}{d\epsilon} \left(\int_{\Omega_{\epsilon}} \rho |\nabla u_{\epsilon}|^{2} + \rho^{-1} u_{\epsilon}^{2} dx \right) \Big|_{\epsilon=0} \\
= \gamma \int_{\Omega} 2\rho \nabla u \cdot \nabla \dot{u} + 2\rho^{-1} u \dot{u} dx + \gamma \int_{\Sigma} \left(\rho |\nabla u|^{2} + \rho^{-1} u^{2} \right) \dot{\mathbf{x}} \cdot \nu dS.$$

168 Integration by parts then gives

169 (2.9)
$$\frac{d}{d\epsilon} \Phi(\Omega_{\epsilon}, f_{\epsilon}) \Big|_{\epsilon=0} = \gamma \int_{\Sigma} \left(\rho |\nabla u|^2 + \rho^{-1} u^2 \right) \dot{\mathbf{x}} \cdot \nu - 2\rho \nabla u \cdot \nu \dot{u} \, dS.$$

Due to the minimality condition $-\rho^2 \Delta u + u = 0$, the interior values of \dot{u} do not enter

172 (2.9). Based on (2.7) and the fact that ν and ν_i have opposite orientation,

173
$$\frac{d}{d\epsilon} \Phi(\Omega_{\epsilon}, f_{\epsilon}) \Big|_{\epsilon=0} = \gamma \sum_{i=1}^{N} \int_{\partial P_{i}} -\left(\rho |\nabla u|^{2} + \rho^{-1} u^{2}\right) \nu_{i} \cdot \dot{\mathbf{x}}_{i}(0) + 2\rho \nabla u \cdot \nu_{i} \nabla u \cdot \dot{\mathbf{x}}_{i}(0) dS$$

6 S.-P. P. FU, R. J. RYHAM, A. KLÖCKNER, M. WALA, S. JIANG, AND Y.-N. YOUNG

174
$$= \gamma \sum_{i=1}^{N} \int_{\partial P_i} \dot{\mathbf{x}}_i(0) \cdot \left[-\rho^{-1} u^2 \mathbf{I} + 2\rho (\nabla u \otimes \nabla u - \frac{1}{2} |\nabla u|^2 \mathbf{I}) \right] \cdot \nu_i \, dS$$
175
$$= -\sum_{i=1}^{N} \int_{\partial P_i} (\dot{\mathbf{c}}_i(0) + \dot{\mathbf{Q}}_i(0) \mathbf{r}_0) \cdot \mathbf{T} \cdot \nu_i \, dS$$
176 (2.10)
$$= -\sum_{i=1}^{N} \left(\dot{\mathbf{c}}_i(0) \cdot \mathbf{F}_i + \mathbf{w}_i \cdot \tau_i^0 \right),$$

- where $\mathbf{w}_i = \langle w_1^i, w_2^i, w_3^i \rangle$ is the axial vector for the skew symmetric tensor $\dot{\mathbf{Q}}_i(0)$.
- In the second to last equation, the minus sign makes the force act in the negative
- direction of the potential gradient. This establishes (2.2) and (2.3).
- In the formulation (2.4), the rigid motions are independent. Consider the case when the rigid motions are uniform, that is, $\mathbf{c}_i(\epsilon) = \mathbf{c}(\epsilon)$ and $\mathbf{Q}_i(\epsilon) = \mathbf{Q}(\epsilon)$ for all
- i = 1, ..., N. Then the solution to the perturbed BVP (2.5, 2.6) satisfies

184 (2.11)
$$u_{\epsilon}(\mathbf{c}(\epsilon) + \mathbf{Q}(\epsilon)\mathbf{X}) = u(\mathbf{X}).$$

185 It follows that $\Phi(\Omega_{\epsilon}, f_{\epsilon}) = \Phi(\Omega, f)$ for all ϵ and, by (2.10), that

186 (2.12)
$$\sum_{i=1}^{N} \dot{\mathbf{c}}(0) \cdot \mathbf{F}_{i} + \mathbf{w} \cdot \tau_{i}^{0} = -\frac{d}{d\epsilon} \Phi(\Omega_{\epsilon}, f_{\epsilon}) \Big|_{\epsilon=0} = -\frac{d}{d\epsilon} \Phi(\Omega, f) \Big|_{\epsilon=0} = 0.$$

Here, $\mathbf{w} = \langle w_1, w_2, w_3 \rangle$ is the axial vector for $\dot{\mathbf{Q}}(0)$. Since $\dot{\mathbf{c}}(0)$ and \mathbf{w} are arbitrary, we have

189 (2.13)
$$\sum_{i=1}^{N} \mathbf{F}_{i} = \mathbf{0}, \quad \sum_{i=1}^{N} \tau_{i}^{0} = \mathbf{0}.$$

- 190 In other words, the net hydrophobic interaction is force and torque free.
- 2.1. Simulations. For the simulations in this paper, the P_1, \ldots, P_N are twodimensional Janus-type particles. The direction vector $\mathbf{d}_i = \langle \cos \theta_i, \sin \theta_i \rangle$ specifies orientation and \mathbf{a}_i is the particle position (e.g. the center of mass, Figure 1). The particle shapes are ellipses with semi-major and semi-minor axes a_i and b_i , respectively. In the case of lipids, $2a_i$ represent lipid length and major axis is parallel to the director and hydrocarbon tail.
 - The material label for the Janus-type particle takes the form

198 (2.14)
$$f(\mathbf{x}) = 1 - \sin^p(\theta), \quad \mathbf{x} \in \partial P_i,$$

- where θ is the angle formed by $\mathbf{x} \mathbf{a}_i$ and \mathbf{d}_i . Accordingly, there is a smooth tran-
- sition in hydrophobicity across the particle [51], with the boundary portion in the
- direction \mathbf{d}_i modeling a hydrophobic tail and the opposite boundary portion mod-
- 202 eling a hydrophilic head. The size of the hydrophobic region grows with the even
- 203 integer parameter p. Finally,

$$\tau_i = \tau_i^0 - \mathbf{a}_i \times \mathbf{F}_i$$

- is the two-dimensional (scalar) torque about the position a_i .
- For small but fixed separations between particles, our numerical scheme accurately resolve the field u without an undue cost increase due to refinement; we postpone a

detailed discussion of the method and involved cost to Section 6. Dynamically, the forces (2.2) bring the coarse-grained lipid particles into contact. An excluded volume repulsion prevents near-contact between particles [64]. For two circular particles, the interaction is

212 (2.16)
$$\mathbf{F}_{ij}^{\text{rep}} = c_0 \frac{q}{(|\mathbf{a}_i - \mathbf{a}_j| - (b_i + b_j))^{q+1}} \frac{\mathbf{a}_i - \mathbf{a}_j}{|\mathbf{a}_i - \mathbf{a}_j|}, \quad i \neq j.$$

We fix the order q = 3 (q = 4 in three-dimensions) and use the parameter c_0 to control the strength of repulsion. For ellipses of eccentricity close to zero, we approximate the excluded volume repulsion using three circular particles placed along the major axes, as described in Supplementary Material, Section S1. In the sequel,

217 (2.17)
$$\mathbf{F}_{i}^{\text{rep}}, \quad \tau_{i}^{\text{rep}}, \quad \Phi_{\text{rep}},$$

denote the excluded volume force, torque and repulsion potential, respectively. The total potential that includes hydrophobic attraction and steric repulsion is

$$\Phi_{\text{Total}} = \Phi + \Phi_{\text{rep}}.$$

For the simulations, we assume translation invariance in the z-direction. Figures 5 and 8 give values in $k_{\rm B}T$ per length since the two-dimensional simulations are for the cross-section of a three-dimensional bilayer. All other physical parameters correspond to their usual three-dimensional value.

We use $2a_i = 2.5$ nm as a representative phospholipid length [3], the screening length $\rho = 2.5$ nm [17, 48, 63, 35, 76], and $c_0 = 0.5$ pN nm⁴ for the inter-particle repulsion. Bilayers containing different single pure components give various interfacial tension γ values which are within the range of 0.7 - 5.3 pN nm⁻¹ [45, 65]. We find that the mechanical moduli calculated from our simulation data are in good agreement with results in the experimental literature when the interfacial tension $\gamma = 4.1$ pN nm⁻¹. Coincidentally, this value corresponds to a specific lipid composition DPoPC:SM:Chol in bilayer membrane [24, Table 1].

Our experiences show that the computational cost to maintain the same numerical accuracy in solving the boundary value problem (1.3) grows only moderately when going from circular to elliptical model particles. For instance, ellipses with $a_i/b_i=3$ require 60 % more grid points than for $a_i/b_i=1$. At the same time, ellipses afford flexibility in terms of dimensions that determine physical properties of bilayer. However, we remark that rather than representing a physical lipid or collection of lipids, the model particle discretizes the mean lipid position and orientation but without the mesh associated with finite element methods, for example [2, 72]. Similarly, the gap region between neighboring particles indicates a hydrophobic zone and not an intervening water.

3. Bilayer Elasticity. We compare our two-dimensional equilibrium configurations to those found in membrane continuum mechanics. In large particle number HADF simulations, particles bring opposing hydrophobic regions into contact, forming two abutting monolayers of a bilayer. Continuum theory describes monolayers using a director field ${\bf d}$ to track lipid orientations, along with a field ${\bf n}$ given by the monolayer surface normal (Figure 3A), and quantifies monolayer energy using a Helfrich Hamiltonian

250 (3.1)
$$\int_{\mathcal{C}} \frac{1}{2} k_{\rm B} \left[\left(\text{Div } \mathbf{d} + k_0 \right)^2 - k_0^2 \right] + \frac{1}{2} k_{\theta} |\mathbf{d} \times \mathbf{n}|^2 \, ds.$$

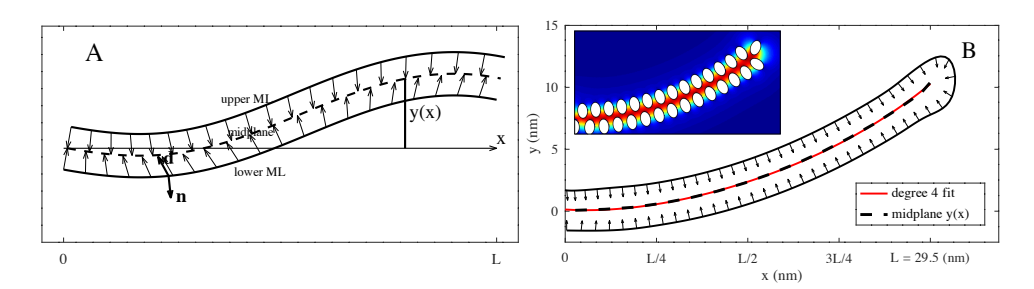


FIG. 3. Panel A depicts a bilayer, with its upper and lower monolayers (solid curves) and midplane (dashed curve). The director field ${\bf d}$ points in the direction of the lipid tails and the normal ${\bf n}$ points outward from bilayer core. When deformations and tilt are small ($|y'| \ll 1$, $|{\bf d} \times {\bf n}| \ll 1$) energy is quantified in terms of the midplane has the height function y(x). Panel B has the equilibrium configuration Janus-type amphiphilic particles with uniform loading and a clamped boundary condition. Fitting (3.4) to the midplane (dashed curve) yields the bending modulus $k_B = 8.51~k_BT$. In Panel B (inset), enumerating counterclockwise from the bottom left, particles satisfy $x_1 = 0$, $x_{16} = 1.5$, $\theta_1 = \pi/2$, $\theta_{16} = -\pi/2$ and $y_1 = 0$. The parameters are $\gamma = 4.1~pN~nm^{-1}$, $\rho = 2.5~nm$, $c_0 = 0.5~pN~nm^{-4}$ and $k = 0.0116~pN~nm^{-2}$. The ellipses have $a_i = 1.25~nm$ and $b_i = 0.8~nm$.

The curve \mathcal{C} tracks the cross-section of the monolayer neutral surface. The integrand in (3.1) contains the splay distortion Div \mathbf{d} with bending modulus $k_{\rm B}$, and the tilt deformation $\mathbf{d} \times \mathbf{n}$ with tilt modulus k_{θ} [57]. The parameter k_0 is spontaneous curvature [71, 42, 75]. Since we are assuming translational invariance in the z-direction, the twist Curl \mathbf{d} and saddle-splay det D distortions are absent from [33, 76], and (3.1) behaves as an energy density per length.

Consider a planar bilayer subject to a uniform vertical load. The bilayer is clamped and horizontal at one end and the restoring force of bending in the free part of the bilayer opposes the load. Taking $\bf d$ parallel to $\bf n$ and assuming a small deformation gives the appropriate functional

261 (3.2)
$$\int_0^L k_{\rm B}(y'')^2 - ky \, dx, \quad y(0) = y'(0),$$

where y(x) is the height function for the bilayer midplane (Figure 3A, dashed curve), Div $\mathbf{d} = \pm y''$ and k is the load strength. The summation of the monolayer energies (3.1) with opposite normals leads to the cancelation of the spontaneous curvature terms in (3.2).

Minimizers of (3.2) satisfy the boundary value problem

267 (3.3)
$$2k_{\rm B}y^{(4)} = k, \quad y(0) = y'(0) = y''(L) = y^{(3)}(L) = 0.$$

268 We find the solution

251

252

253

254 255

256

257

258

259

260

266

269 (3.4)
$$y(x) = \frac{kL^4}{2k_B} \left[\frac{1}{24} \left(\frac{x}{L} \right)^4 - \frac{1}{12} \left(\frac{x}{L} \right)^3 + \frac{1}{4} \left(\frac{x}{L} \right)^2 \right].$$

Thus, we can determine $k_{\rm B}$ from curves of the form (3.4) whenever L and k are given.

The inset in Figure 3B shows a HADF equilibrium configuration used to determine $k_{\rm B}$. The N=30 particles minimize the modified functional

$$\Phi_{\text{Total}} - \sum_{i=1}^{N} \tilde{k} y_i,$$

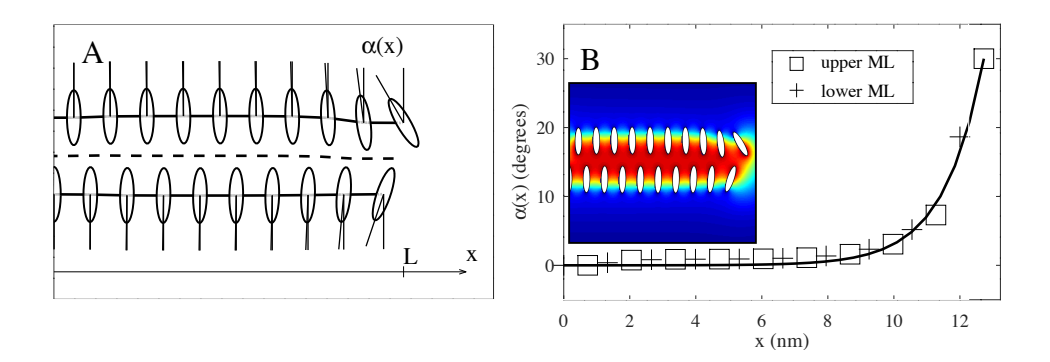


Fig. 4. The monolayers in panel A are flat and tilt is nonzero. The horizontal coordinate x runs between 0 and the length of bilayer, L, and the function $\alpha(x)$ measure the angle between $-\mathbf{d}$ and the unit normal. The boundary conditions for (3.6) are $\alpha_0 = 0^\circ$ and $\alpha_1 = 30^\circ$. In panel B, the + and \square symbols are the angles at the particle centers. The parameters are $\gamma = 4.1$ pN nm⁻¹, $\rho = 2.5$ nm, $c_0 = 0.5$ pN nm⁻⁴, and k = 0.0116 pN nm⁻². The ellipses have $a_i = 1.25$ nm and $b_i = 0.3125$ nm.

where the $\tilde{k} = Lk/N$ is the discrete load strength coming from quadrature of the integral (3.2) with N many particles. To achieve minimality, the particles start in the shape of a flat bilayer, and then migrate upward following steepest gradient for (3.5).

The main figure in Figure 3B depicts the monolayer neutral surface (solid curve), midplane (dashed curve) and the lipid directors interpolated from the discrete particle positions and orientations (of the inset). The directors are everywhere normal to the neutral surface and the deformations are small. This justifies applying the zero-tilt, small-deformation solution (3.4). Fitting a 4th degree polynomial to the midplane curve (Figure 3B, red curve) supplies the coefficient $(kL^4/2k_B)$ of (3.4). Combining the coefficient with simulation values for L and k (Figure 3B, caption) yields $k_B = 8.51 \text{ k}_B\text{T}$. This value for the bending modulus is for ellipses using p = 6 in the hydrophobicity boundary condition (2.14). To assess how bilayer rigidity depends on the material label, we considered the energy minimization with p = 2, which gave $k_B = 13.54 \text{ k}_B\text{T}$. We conclude that under HADF, particle configurations behave like an elastic material. The associated bending modulus grows with symmetry in the hydrophobic surface label, e.g. k_B was largest for p = 2 where the label is symmetric across $\theta = \pi/2$.

Now we consider a flat monolayer with nonzero tilt (Figure 4A). The splay distortion comes from changes in the angle $\alpha(x)$ between the director **d** and the vertical. For small angles, the monolayer energy (3.1) becomes

294 (3.6)
$$\int_0^L \frac{1}{2} k_{\rm B} (\alpha')^2 + \frac{1}{2} k_{\theta} \alpha^2 dx, \quad \alpha(0) = \alpha_0, \quad \alpha(L) = \alpha_1.$$

Note that we have left off the null-Lagrangian term $k_{\rm B}k_0\alpha'$ from this expression since $k_{\rm B}$, k_0 and the boundary data α_0 and α_1 are constants. Assuming $\alpha(0) = 0$, minimizers of (3.6) take the form

298 (3.7)
$$\alpha(x) = \alpha_1 \frac{\sinh(x/\kappa)}{\sinh(L/\kappa)},$$

where $\lambda = \sqrt{k_{\rm B}/k_{\theta}}$ is the tilt decay length [45]. Figure 4B shows the data (plusses and squares) for the HADF equilibrium configuration with fixed endpoint angles.

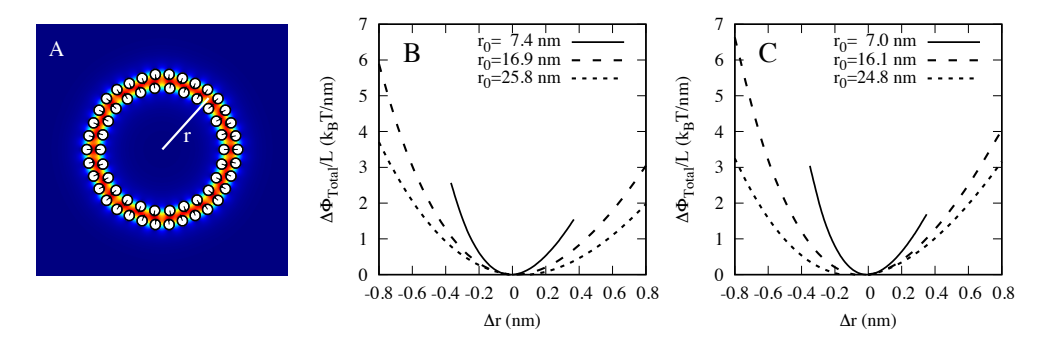


FIG. 5. Panel A shows the activity field for the cross-section of a cylindrical bilayer. The radius measures from the center to the midplane. Panels B and C plot the change in energy $\Delta\Phi_{Total} = \Phi_{Total}(r) - \Phi_{Total}(r_0)$ per length of the cylinder under stretching and compression: $\Delta r = r - r_0$. Equilibrium radius r_0 decreases with c_0 ; the curves are for $c_0 = 0.5$ pN nm⁴ in panel B, and $c_0 = 0.25$ pN nm⁴ in panel C ($\gamma = 4.1$ pN nm⁻¹, in both panels). The solid, dashed and dotted curves use N = 26, N = 60 and N = 92 particles, and collapse onto a single curve when multiplied by r_0 .

The solid curve fits (3.7) to the angle data for the value $\lambda = 1.2$ nm. This value is consistent with experimental and theoretical measurements of the bending and tilt moduli [57, 41].

In HADF, tilt dissipation is a consequence of repulsion between rod-like particles. The ellipses in Figure 4 are elongated and have $a_i/b_i = 4$. When the particles are more circular $(a_i/b_i \sim 1)$, the bulk particles ignore endpoint orientations and the angle function $\alpha(x)$ is non-monotonic in x.

Finally, we discuss simulation data for stretching. Consider the stretching energy of a cylindrical bilayer:

310 (3.8)
$$k_{\rm A} \frac{(A-A_0)^2}{A_0},$$

 where $A = 2\pi r L$, r is the midplane radius, L is the cylinder length (in the z-direction) and A_0 is the area at rest. The stretching modulus k_A is for a single monolayer and (3.8) accounts for the energy of the inner and outer monolayer leaflets of the cylinder. Manipulation experiments give k_A in the range 30 – 40 k_B T nm⁻² [56, 57].

To measure a stretching modulus, we form the circular cross section of cylinder of radius r (Figure 5A). The equilibrium shape is nearly circular (so long as there is a consistent number of particles in each leaflet) and the shape obtains an equilibrium radius r_0 once compression and attraction are in balance. We use a harmonic bond to move r away from equilibrium and record the change in energy (Figure 5BC).

The three curves in Figure 5B collapse onto a single curve when multplied by r_0 . Fitting to $cr_0(r-r_0)^2$ and comparing with (3.8) yields $k_{\rm A}=33.4~{\rm k_BT~nm^{-2}}$, 35.3 ${\rm k_BT~nm^{-2}}$ and 35.9 ${\rm k_BT~nm^{-2}}$ for the three radii respectively. The proximity of these three values suggests that HADF possesses a stretching modulus independent of particle number. Moreover, the attraction $\gamma=4.1~{\rm pN~nm^{-1}}$ and repulsion parameters $c_0=0.5~{\rm pN~nm^4}$ yield a consistent and physically realistic stretching modulus, around $k_{\rm A}=35~{\rm k_BT~nm^{-2}}$. As an illustration, the curves in Figure 5C are for the same tension parameter and half the repulsion strength. There is an overall reduction in the equilibrium radii with the decreased repulsion, and an increase in the stretching moduli $k_{\rm A}$ to 40.310 $k_{\rm B}$ T nm⁻², 40.083 $k_{\rm B}$ T nm⁻² and 39.393 $k_{\rm B}$ T nm⁻² for the three curves respectively.

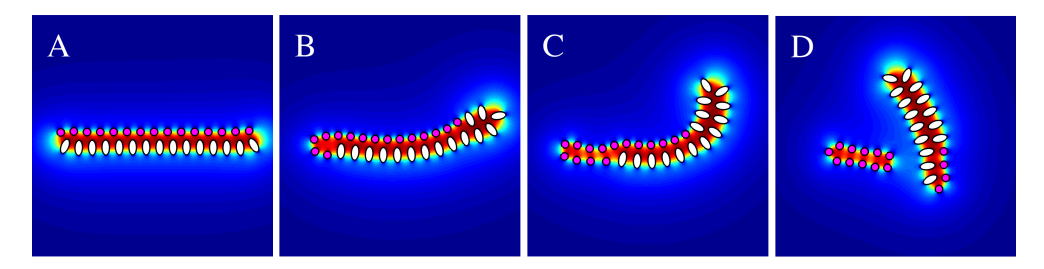


FIG. 6. Panels A-D show the spontaneous sorting and eventual fission of a planar bilayer mixture of small circular particles (magenta) and elliptical particles (white). The monolayer consisting of smaller, circular particles spontaneously migrates from the bilayer edge, and eventually breaks off forming forming its own bilayer. The bending in panels B and C suggests that the smaller, circular particles have a spontaneous curvature more negative than for the larger, elliptical particles. The parameters are $\gamma = 4.1 \text{ pN nm}^{-1}$, $\rho = 2.5 \text{ nm}$ and $c_0 = 0.5 \text{ pN nm}^{-4}$ The ellipses have p = 6, $a_i = 1.25 \text{ nm}$ and $b_i = 0.6225 \text{ nm}$ while the circles have p = 2, $a_i = b_i = 0.6225 \text{ nm}$.

HADF yields physically realistic continuum-like bilayer morphologies and these particle configurations possess elastic properties of lipid bilayer. The HADF can also handle topological changes and mixtures in a straightforward manner. Figure 6 illustrates the gradient descent dynamics of a lipid mixture between small, circular and large, elliptical particles. Under hydrophobic attraction and excluded volume repulsion, the particle mixture segregates into two bilayers of more uniform composition. Diffusive interface and level-set approaches have dealt with the problem of mixtures by defining transport equations for each lipid species density [49, 55, 25].

Hemifusion is one of the key intermediates of membrane fusion involving a Y-shaped junction between three bilayers [9](see Figure 8, Panel C). Pioneering work by Promilsow, K. and coworkers [12, 13] has lead to functionalized Cahn-Hilliard, diffusive interface energies that exhibit freestanding elastic phases, including the Y-shaped junction [43, 21]. It is still unclear whether the HADF formulation of the present work is more or less efficient than a functionalized Cahn-Hilliard approach for capturing the granular energetic details of fusion [72].

4. Hydrodynamics of amphiphilic particles in a viscous solvent. To define particle velocities, we assume that the amphiphilic particles are immersed in an incompressible viscous fluid in the Stokes flow regime. Then all the particles interact with each other through both hydrophobic forces and Stokesian hydrodynamic interactions. The two-dimensional particles P_i have the translational and angular velocities

352 (4.1)
$$\frac{d\mathbf{a}_i}{dt} = \mathbf{v}_i, \quad \frac{d\theta_i}{dt} = \omega_i,$$

 $i=1,\ldots,N$. For the amphiphilic particles in a solvent, the forces \mathbf{F}_i , $\mathbf{F}_i^{\mathrm{rep}}$ and torques τ_i , τ_i^{rep} are calculated from (2.2) and (2.15), respectively, The velocities \mathbf{v}_i and ω_i are coupled together through the fluid velocity \mathbf{u} and pressure p satisfying

$$-\mu \Delta \mathbf{u} + \nabla p = 0,$$

$$\nabla \cdot \mathbf{u} = 0, \quad \text{in } \Omega,$$

$$\mathbf{u} \to 0 \quad \text{as } |\mathbf{x}| \to \infty,$$

$$\mathbf{u}(\mathbf{x}) = \mathbf{v}_i + \omega_i (\mathbf{x} - \mathbf{a}_i)^{\perp}, \quad \mathbf{x} \in \partial P_i,$$

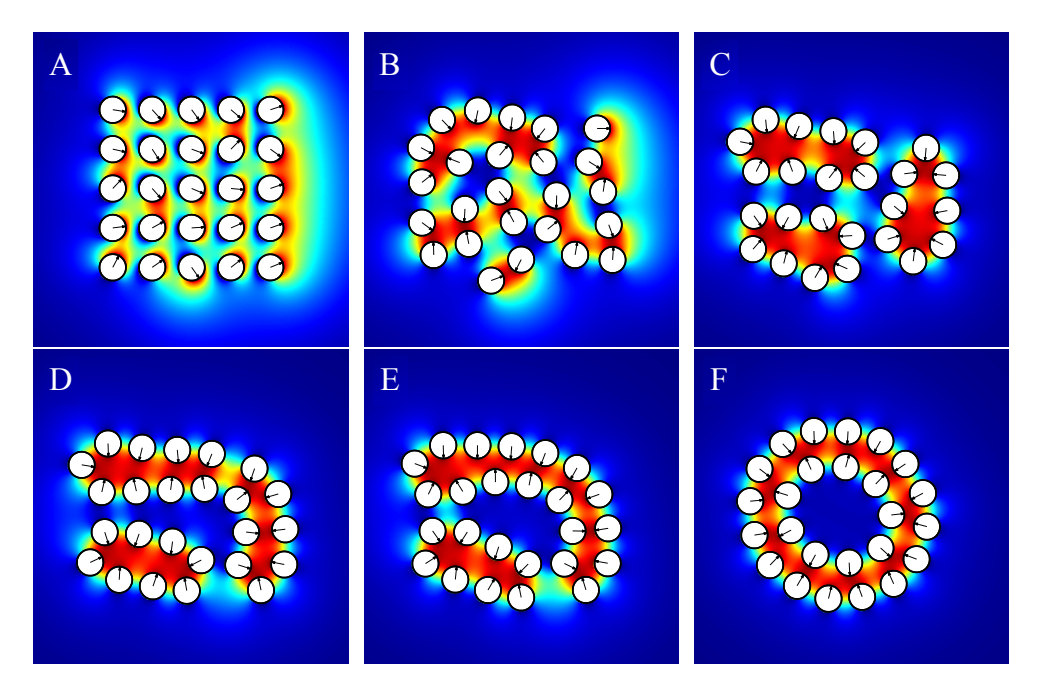


Fig. 7. For large system simulations, particles self assemble into bilayer-like shapes and then eventually a cylindrical bilayer. Panels A–F are for 0, 3.8, 19, 76, 114 and 228 ns, respectively; step size $\Delta T = 1.0[T] \approx 0.38$ ns. The configuration in panel F evolves very slowly to one that is slightly more circular.

with fluid viscosity μ and subject to the stress balance conditions

358 (4.3)
$$\int_{\partial P_i} \mathbf{S} \cdot \mathbf{n} \, dS = \mathbf{F}_i + \mathbf{F}_i^{\text{rep}}, \quad \int_{\partial P_i} (\mathbf{x} - \mathbf{a}_i) \times \mathbf{S} \cdot \mathbf{n} \, dS = \tau_i + \tau_i^{\text{rep}}.$$

359 From (2.13) these particle forces and torques also satisfy the force-free and torque-

360 free conditions, guaranteeing the existence of an integral solution for the many-body

mobility problem. The evolution equations (4.1-4.3) satisfy the dissipation relation

362 [47]

363 (4.4)
$$\frac{d}{dt}\Phi_{\text{Total}} + \int_{\mathbb{R}^n} \frac{1}{2}\mu |\nabla \mathbf{u} + \nabla \mathbf{u}^T|^2 dx = 0.$$

In two dimensions, the kernels of single and double layer potentials for solving the Stokes equation are the stokeslet and stresslet

$$G_{i,j}^{\text{Stokeslet}}(\mathbf{x}, \mathbf{y}) = \frac{1}{4\pi\mu} \left[\log |\mathbf{x} - \mathbf{y}| \delta_{ij} + \frac{(x_i - y_i)(x_j - y_j)}{|\mathbf{x} - \mathbf{y}|^2} \right],$$

$$\mathbf{T}_{i,j,k}^{\text{Stresslet}}(\mathbf{x}, \mathbf{y}) = -\frac{1}{\pi\mu} \frac{(x_i - y_i)(x_j - y_j)(x_k - y_k)}{|\mathbf{x} - \mathbf{y}|^4},$$

respectively, with i, j, k = 1, 2. For a velocity surface density μ , the stresslet satisfies the jump across the boundary

369 (4.6)
$$\lim_{\mathbf{z} \to \mathbf{x}^{\pm}} \mathbf{f}_{i,\pm}(\mathbf{z}) = \mp \frac{1}{2} \boldsymbol{\mu}_i(\mathbf{x}) + \text{p.v.} \int_{\partial P_i} \mathbf{T}_{i,j,k}^{\text{Stresslet}}(\mathbf{x}, \mathbf{y}) \boldsymbol{\mu}_j(\mathbf{y}) ds_{\mathbf{y}},$$

where \mathbf{f}_i denotes the surface traction of on particle P_i . Following [67], one views the external force and torque due to hydrophobic attraction as an incident field with stress (2.3). The scattered field is then the net force and torque due to fluid mobility. If we split densities into $\boldsymbol{\sigma}^{\mathrm{inc}}(\mathbf{x}) = \{\boldsymbol{\sigma}_1^{\mathrm{inc}}, \dots, \boldsymbol{\sigma}_N^{\mathrm{inc}}\}$ and $\boldsymbol{\mu}(\mathbf{x}) = \{\boldsymbol{\mu}_1, \dots, \boldsymbol{\mu}_N\}$, then the particle dynamics (4.7) can be obtained by evaluating a single layer potential for corresponding densities $\boldsymbol{\sigma}$ and $\boldsymbol{\mu}$.

376 (4.7)
$$\mathbf{u}(\mathbf{x}) = \sum_{j=1}^{N} \int_{\partial P_j} G_{i,j}^{\text{Stokeslet}}(\mathbf{x}, \mathbf{y}) [\boldsymbol{\sigma}_j^{\text{inc}} + \boldsymbol{\mu}_j](\mathbf{y}) ds_{\mathbf{y}}$$
$$= \mathbf{v}_i + \omega_i (\mathbf{x} - \mathbf{a}_i)^{\perp} \quad \forall \mathbf{x} \in \partial P_i,$$

377 where

403

$$\mathbf{v}_{i} = \frac{d\mathbf{a}_{i}}{dt} = \frac{1}{|\partial P_{i}|} \int_{\partial P_{i}} \mathbf{u}(\mathbf{y}) ds_{\mathbf{y}}, \quad |\partial P_{i}| = \int_{\partial P_{i}} ds_{\mathbf{y}},$$

$$\omega_{i} = \tau^{-1} \int_{\partial P_{i}} (\mathbf{y} - \mathbf{a}_{i}) \times \mathbf{u}(\mathbf{y}) ds_{\mathbf{y}}, \quad \tau = \int_{\partial P_{i}} |\mathbf{y} - \mathbf{a}_{i}|^{2} ds_{\mathbf{y}}.$$

For the time-marching scheme, we solve the mobility problem for the particle translation and rotation velocities. We then update the particle centers and orientations using a forward Euler scheme. Algorithm 5.1 provides the time-marching details.

Non-dimensionalizing (1.1) with characteristic length 1.25 nm, fluid viscosity $\mu=1$ cP and interfacial tension $\gamma=4.1$ pN nm⁻¹ gives the characteristic time $[T]=\mu a/\gamma\approx 3.82\times 10^{-10}s$. As an illustration, the evolution in Figure 1 is for 100 time steps with time step size $\Delta T=1.0[T]$. The time for self assembly of a few particles from an initially random configuration is thus on the order of a nanosecond. This is consistent with times scales for lipid rearrangements in MD simulation [10]. Supplementary Materials Movie 1 shows the self-assembly process for three particles.

Bilayer configurations form when we increase the number particles in the simulation. Figure 7A has 25 Janus-type particles placed on a square grid. The initial orientations θ_i are normally distributed about $\theta=0$. Within ten time steps (Figure 7B), the particles rapidly rotate to pair their hydrophobic interfaces with that of neighboring particles. Pairings continue to merge forming groups of eight or nine particles (Figure 7C). These groups stack together to form an arched bilayer shape resembling the cross-section of a stomatocyte (Figure 7E). Figure 7F clearly shows an inner and outer monolayer configuration a cylindrical bilayer.

Supplementary Materials Movie 2 illustrates the self-assembly process for Figure 7A–F. As part of computational complexity test, we have calculated particle dynamics for larger systems and Supplementary Materials Movie 3 shows the results for 100 particles.

Is it possible to replace the detailed hydrodynamic interaction with one that uses a constant coefficient drag coefficient law? The latter also exhibits particle self-assembly and avoids the computational cost of solving an additional mobility problem. Moreover, the constant coefficient case drag laws can closely replicate the hydrodynamic interaction case when particles are dispersed (see Supplementary Material, Section S2.3). Nevertheless, numerical experiments show that the choice of dissipative mechanism is consequential to the time course. For example, Figure 7F and Figure 8B compare the two different end-states resulting from a identical initial configurations

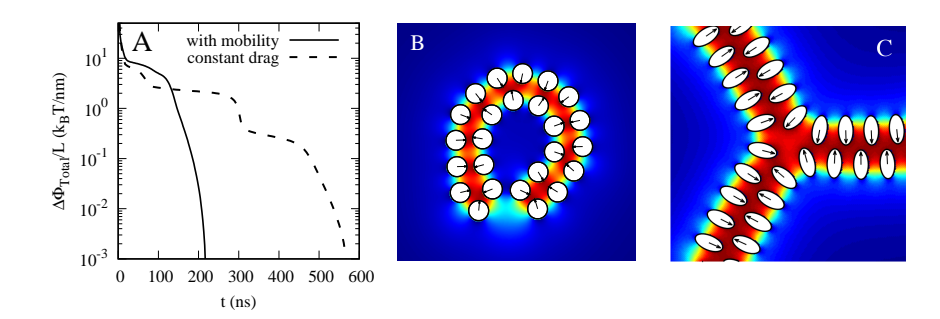


Fig. 8. Panel A plots the change in energy Φ per length (solid curve) for the evolution Figure 7A–F. The initial rapid decrease over 0 ns < t < 10 ns corresponds to Figure 7A–B. The moderate decrease over 10 ns < t < 150 ns is for Figure 7C–E. Energy decreases very slowly over 150 ns < t < 600 ns, where the bilayer evolves from a somewhat elliptical cross-section (Figure 7F) to one that is almost perfectly circular. The dashed curve gives corresponding values for a constant drag coefficient evolution: its end-state is in panel B. In panel C, the free ends of three bilayers have merged into an equilibrium, Y-shaped junction.

for a viscous fluid and for a constant drag law, respectively. The difference lies in the number of particles contained in the inner leaflet and this has determined whether or not the bilayer closes.

 5. Boundary Integral Equation Formulation. In this section, we present a second kind integral equation formulation for the exterior Dirichlet problem (1.3). The domain Ω is the exterior domain, meaning that its complement Ω^c (the collection of particles) is compact.

There are a number of numerical methods for solving the exterior problem (1.3). These include finite difference methods, finite element methods, and boundary integral equation (BIE) methods. The BIE methods are perhaps the most suitable since they represent the solution via layer potentials with an unknown density only on the boundary. This reduces the dimension of the problem by one and leads to a much smaller linear system. Another advantage is that the integral representation automatically satisfies the governing partial differential equation and the boundary condition at infinity. Thus, there is no need to truncate the computational domain and impose artificial boundary conditions, as would be the needed with the finite element and finite difference approaches. Finally, when combined with high-order quadratures and fast algorithms such as the fast multipole methods [31, 32], the BIE formulation leads to a high-order numerical algorithm with optimal computational complexity.

Before describing the method, we first consider whether the far-field condition in (1.3) is sufficient to determine a unique solution. As mentioned in Section 1, the functional $I[\cdot]$ has a unique minimizer in \mathcal{A} . The minimizer u satisfies $0 \leq u(x) \leq 1$ for all $x \in \Omega$. To see why these bounds holds, consider a truncated version $\tilde{u} = \max\{0, \min\{1, u\}\}$ of u. Because $0 \leq f \leq 1$ on Σ , $\tilde{u} \in \mathcal{A}$. Lastly, $I[\tilde{u}] \leq I[u]$ by inspection, and $I[u] \leq I[\tilde{u}]$ by minimality of u. This implies that $I[\tilde{u}] = I[u]$, and since u is the unique minimizer, we have $u = \tilde{u}$.

To obtain a far-field decay condition, select a sufficiently large distance D > 0 from Ω^c . Let x be such that $d(x, \Omega^c) > D$. By a change of coordinates, we may assume that x is the origin $(0, \ldots, 0)$ and that Ω^c lies in the set $\{(x_1, \ldots, x_n) : x_n \leq -D\}$. In

440 this coordinate system, consider the function

$$v_{\epsilon}(x_1, \dots, x_n) = \frac{\cosh(x_n/\rho)}{\cosh(D/\rho)} + \epsilon \sum_{i=1}^{n-1} \cosh(x_i/\rho), \quad \epsilon > 0.$$

- 442 Then $-\rho^2 \Delta v_{\epsilon} + v_{\epsilon} = 0$ and $v_{\epsilon} \geq 1$ on Σ (since x_n is less than -D there), and $v_{\epsilon} \to \infty$
- 443 as $|(x_1,\ldots,x_n)|\to\infty$. Next, consider the function $g=v_\epsilon-u$. We have $g\geq 0$ on
- 444 Σ and $g \geq 0$ for all sufficiently large (x_1, \ldots, x_n) (since $v_{\epsilon} \to \infty$ and u is bounded
- everywhere between 0 and 1).
- From the weak maximum principle [26, Cor. 3.2, assuming $f \in C(\Sigma)$], we have
- 447 $g \ge 0$ in Ω . It follows that $v_{\epsilon} \ge u$ in Ω . Finally, letting $\epsilon \to 0$, we conclude that

448 (5.1)
$$0 \le u(x) \le v_{\epsilon}(x) < 2\exp(-D/\rho)$$

- 449 as soon as $\epsilon > 0$ is sufficiently small.
- The problem (1.3) thus has at least one solution (vanishing at infinity), namely the
- variational one. But since the domain Ω is non-compact, it is in principle possible that
- 452 (1.3) has multiple solutions vanishing at infinity with different rates. The following
- Liouville-type result shows that this is not the case. In fact, we get uniqueness even
- 454 if we replace the zero far-field condition with the power growth condition $u = O(|x|^p)$
- 455 as $x \to \infty$.
- LEMMA 5.1. The exterior problem (1.3) has at most one solution.
- 457 Proof. Suppose that (1.3) has two solutions u_1 and u_2 . Let $w = u_1 u_2$ and 458 define

459
$$E(r) = \int_{\Omega \cap \mathbf{B}} \frac{1}{2} w^2 \, dx, \qquad E: [0, \infty) \to [0, \infty),$$

- 460 where B_r is the ball of radius r centered at the origin. Select r_0 positive and sufficiently
- 461 large so that $\Omega^c \subset B_{r_0}$.
- The function E(r) is infinitely differentiable on (r_0, ∞) since any solution of (1.3)
- 463 is smooth in Ω . Using w = 0 on Σ and (1.3), it follows that

464 (5.2)
$$E''(r) = \frac{n-1}{r}E'(r) + \frac{1}{\rho^2}E(r) + \int_{\Omega \cap B_r} |\nabla w|^2 dx, \quad r_0 < r < \infty.$$

Since E is nondecreasing, by definition, we get

466
$$E''(r) \ge \rho^{-2} E(r), \quad r_0 < r < \infty.$$

467 Let $F(r) = \frac{1}{2}E(r_0) \exp((r - r_0)/\rho)$. We claim that

468 (5.3)
$$F(r) \le E(r), \quad r_0 \le r < \infty.$$

- To form the comparison argument, suppose to the contrary that E(r) is not every-
- 470 where greater than or equal to F(r). Then $E(r_0) > 0$ and there is $r_* > r_0$ with
- 471 $E'(r_*) \leq F'(r_*)$ and F(r) < E(r) for $r_0 \leq r < r_*$. But then,

472
$$E'(r_*) \le F'(r_*) = \int_{r_0}^{r_*} \rho^{-2} F(r) \, dr < \int_{r_0}^{r_*} \rho^{-2} E(r) \, dr \le E'(r_*) - E'(r_0).$$

These inequalities are in contradiction since $E'(r_0)$ is nonnegative.

16 S.-P. P. FU, R. J. RYHAM, A. KLÖCKNER, M. WALA, S. JIANG, AND Y.-N. YOUNG

Thus, if u_1 and u_2 are two solutions of (1.3), then according to (5.3) there are one of two possibilities: either $E(r_0) = 0$ or one of the solutions has exponential growth.

The vanishing condition $u \to 0$ as $x \to \infty$ rules out the latter case and so $E(r_0)$ must be zero. Since r_0 was arbitrary, u_1 and u_2 are identical.

In two dimensions, the equation $-\rho^2 \Delta u + u = 0$ has the free-space Green's function (also called fundamental solution)

480 (5.4)
$$G(x,y) = \frac{1}{2\pi} K_0(|x-y|/\rho), \quad x,y \in \mathbb{R}^2,$$

where K_0 is the zeroth order modified Bessel function of the first kind [62]. For a Lipschitz domain Ω in \mathbb{R}^2 with boundary Σ , the space $L^2(\Sigma)$ denotes all square integrable functions on Σ . Given a function $\sigma \in L^2(\Sigma)$, we define the single layer potential by the formula

485 (5.5)
$$S[\sigma](x) = \int_{\Sigma} G(x, y) \sigma(y) ds_y,$$

and the double layer potential by the formula

487 (5.6)
$$\mathcal{D}[\sigma](x) = \int_{\Sigma} \frac{\partial G(x,y)}{\partial \nu(y)} \sigma(y) ds_y,$$

where $\nu(y)$ is the unit outward normal vector with respect to Ω^c . It is well-known from classical potential theory [44] that the single layer potential is continuous and the double layer potential exhibits a jump across the boundary. To be more precise, when z approaches a point $x \in \Sigma$ nontangentially, the limits of $\mathcal{S}[\sigma]$ and $\mathcal{D}[\sigma]$ exist and are given by the following formulas:

493 (5.7)
$$\lim_{z \to x^{\pm}} \mathcal{S}[\sigma](z) = S[\sigma](x) = \int_{\Sigma} G(x, y) \sigma(y) ds_y,$$

494 and

495 (5.8)
$$\lim_{z \to x^{\pm}} \mathcal{D}[\sigma](z) = (\pm \frac{1}{2}I + D)[\sigma](x) = \pm \frac{1}{2}\sigma(x) + \text{p.v.} \int_{\Sigma} \frac{\partial G(x,y)}{\partial \nu(y)} \sigma(y) ds_y,$$

for almost every point $x \in \Sigma$. Here $z \to x^{\pm}$ implies that z approaches x from the exterior(+) or the interior(-) of Ω^c , respectively. It is also well-known that both the single layer operator $S: L^2(\Sigma) \to L^2(\Sigma)$ and the double layer operator $D: L^2(\Sigma) \to L^2(\Sigma)$ are compact when the boundary Σ is C^1 .

We will represent the solution to (1.3) with the double layer potential representation:

$$502 \quad (5.9) \qquad \qquad u(x) = \mathcal{D}[\sigma](x).$$

The jump relation of the double layer potential (5.8) leads to the following boundary integral equation on the unknown density σ :

505 (5.10)
$$\frac{1}{2}\sigma(x) + D[\sigma](x) = f(x), \quad x \in \Sigma.$$

Algorithm 5.1 Particle Updates by Exterior Screened Laplace BVP

- 1: Set the particle centers $\mathbf{a}_i \in \mathbb{R}^2$ and orientations $\theta_i \in \mathbb{R}$, boundary condition f(x) and time step size Δt
- 2: Determine the discretization on the boundary Σ and construct the double layer potential $\mathcal{D}[\sigma](x)$.
- 3: **for** $t = t_0 : t_{end}$ **do**
- 4: Use GMRES iterative method to solve the unknown density σ in (5.10).
- 5: Use the solved σ to obtain the screend Laplace equation solution u and calculate ∇u .
- 6: Calculate inter-molecular forces (2.2) and (2.16).
- 7: Use GMRES iterative method to solve the unknown density μ in (4.6).
- 8: Solve mobility problemand update particle velocities \mathbf{v}_i and ω_i in (4.7).
- 9: Update particle center positions \mathbf{a}_i and orientations θ_i .
- 10: Update the marching time $t = t_0 + \Delta t$.
- 11: end for
- 12: \mathbf{return} T
- THEOREM 5.2. Suppose that ρ is any positive real number. Then for any $f \in L^2(\Sigma)$, the second kind integral equation (5.10) is uniquely solvable.
- *Proof.* By the Fredholm alternative [44], we only need to show that the only solution to the homogeneous equation

511 (5.11)
$$\frac{1}{2}\sigma(x) + D[\sigma](x) = 0.$$

- 512 is $\sigma \equiv 0$.
- Consider the function u(x) defined by the formula (5.9). It is clear that u satisfies the equation $-\rho^2 \Delta u + u = 0$ in both the exterior domain Ω and the interior domain
- 515 Ω^c , and vanishes at infinity. By the uniqueness of the exterior Dirichlet problem
- 516 (Lemma 5.1), we have $u \equiv 0$ in Ω . Hence,

517 (5.12)
$$\lim_{z \to x^+} \frac{\partial u(z)}{\partial \nu} = 0, \quad x \in \Sigma.$$

- 518 Since the normal derivative of the double layer potential is continuous across the
- 519 boundary [44, gen. of Thm. 6.18], we have

520 (5.13)
$$\lim_{z \to x^{-}} \frac{\partial u(z)}{\partial \nu} = 0, \quad x \in \Sigma.$$

Hence, u in the interior domain Ω^c is the solution to the interior Neumann problem

522 (5.14)
$$-\rho^2 \Delta u + u = 0, \quad u \in \Omega^c, \quad \frac{\partial u}{\partial \nu} = 0, \quad x \in \Sigma.$$

523 Applying Green's first identity, we obtain

$$\int_{\Omega^c} \rho^2 |\nabla u|^2 + u^2 dx = 0.$$

- Thus we have $u \equiv 0$ in Ω^c as well. The jump relation of the double layer potential
- 526 (5.8) leads to

527 (5.16)
$$\sigma(x) = \lim_{z \to x^+} u(z) - \lim_{z \to x^-} u(z) = 0, \quad x \in \Sigma,$$

528 which completes the proof.

18 S.-P. P. FU, R. J. RYHAM, A. KLÖCKNER, M. WALA, S. JIANG, AND Y.-N. YOUNG

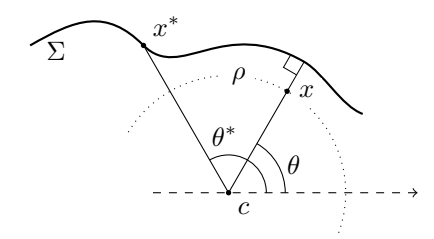


Fig. 9. Geometric situation of a single QBX expansion with sources along the collection of curves Σ , as used in (6.1) and (6.2). Note that the target point x will reside on Σ for the computation of the on-surface value of the layer potential.

Remark 5.3. As pointed out earlier, the screened Laplace equation can be viewed as the Helmholtz equation $\Delta u + k^2 u = 0$ with pure imaginary k. When k is an arbitrary complex number, the so-called Brakhage-Werner representation [5] (also called the Burton-Miller representation [7] in acoustics) represents the solution to the Helmholtz equation via a linear combination of single and double layer potentials

(5.17)
$$u(x) = i\mathcal{S}[\sigma](x) + \mathcal{D}[\sigma](x).$$

It has been shown that the representation (5.17) leads to a uniquely solvable second kind integral equation for any value of $k \in \mathbb{C}$ [59]. Due to the exponential decay of the solution to our exterior problem (1.3), we are able to use the double layer potential alone to represent its solution and still achieve existence and uniqueness of the associated boundary integral equation (5.10).

We would like to point out that when ρ is very large, the formulation (5.17) may lead to a better conditioned linear system than (5.9). There are other second kind integral equation formulations for this problem. For example, one may replace the single layer potential by a collection of point sources inside each particle, where the strength of the point source may be unknown or equal to the average value of the unknown density function on the boundary of each particle. We refer the readers to [29, 30, 36] for details.

6. High-order quadrature and fast algorithms. For the accurate and rapid evaluation of the layer potentials occurring in the previous section, we make use of 'Quadrature by Expansion', or QBX for short [39]. Here we briefly review the QBX scheme for the general Helmholtz kernel and note that the Yukawa kernel (5.4) is simply a special case of the Helmholtz kernel with pure imaginary wave number k. To do so, we cover a neighborhood of the source curve Σ with locally valid ('local') expansions of the potential emanating from the entire source curve Σ . For a collection of on-surface target points (x_i) , expansion centers are chosen as $c_i = x_i + \nu \eta_{x_i}$, where η_x is a scaling factor connected to the local quadrature resolution. See [79] for details of the determination of η_x . Then, for target points $x \in B(c_i, \eta_{x_i})$, the layer potential may be evaluated as

558 (6.1)
$$\phi(x) = \sum_{l=-\infty}^{\infty} \alpha_l J_l(k\rho) e^{-il\theta}$$

where (ρ, θ) denote the polar coordinates of the target point x with respect to the expansion center c, and J_l is the Bessel function of order l (see Fig. 9). For the

single layer potential $S\sigma$, the coefficients α_l in the expansion (6.1) can be computed analytically:

563 (6.2)
$$\alpha_l = \frac{i}{4} \int_{\Sigma} H_l^{(1)}(k|x^* - c|) e^{il\theta^*} \sigma(x^*) dx^*, \qquad (l = -p, -p + 1, \dots, p)$$

where $(|x^* - c|, \theta^*)$ denote the polar coordinates of the point x^* with respect to c. These (now non-singular) integrals for the coefficients α_l are then computed by conventional high-order numerical quadrature. These formulas follow immediately from Graf's addition theorem [62, (10.23.7)],

568 (6.3)
$$H_0^{(1)}(k|x-x^*|) = \sum_{l=-\infty}^{\infty} H_l^{(1)}(k|x^*-c|)e^{il\theta^*}J_l(k|x-c|)e^{-il\theta},$$

This identity applies directly to the Yukawa potentials under consideration here, based on the fact that $K_0(z) = (i\pi/2)H_0^{(1)}(iz)$, cf. [62, (10.27.8)]. Separation-of-variables results similar to Graf's addition theorem hold for Laplace potentials, allowing us to proceed analogously in that case [31]. The QBX procedure described above employs two means of approximation: the truncation of the series expansion, and the computation of the coefficients by numerical quadrature. We give an error result for QBX that accounts for both aspects. For the following result, we consider the case of the double layer and assume c = 0 without loss of generality.

THEOREM 6.1 (QBX truncation and quadrature errors, [16, Thm. 2.5 and (4.6)]). Suppose that Γ is a smooth, bounded curve embedded in \mathbb{R}^2 , such that $B_{\eta_x}(0) \cap \Gamma = \emptyset$, but $\rho e^{i\theta} \in \overline{B}_{\eta_x}(0) \cap \Gamma$. Assume the geometry Γ is discretized using q point composite Gauss-Legendre panels of uniform length h, with a total of n points.

For $k \in [0, \infty)$, N a positive integer, and $\beta > 0$, there are constants $C'_{N,\beta,\Gamma}(k)$ and $C''_{q,\Gamma}(k)$, so that if $\sigma \in C^{N,\beta}(\Gamma)$, then

584 (6.4)
$$\left| \lim_{r \to \rho^{-}} \int_{\Gamma} \frac{\partial G(re^{i\theta}, y)}{\partial \nu(y)} \sigma(y) ds(y) - \sum_{l=1-N}^{N-1} Q_{q}(\alpha_{l}) J_{l}(k\rho) e^{-il\theta} \right|$$
585
$$\leq C'_{N,\beta,\Gamma}(k) \rho^{N} \|\sigma\|_{C^{N,\beta}(\Gamma)} + C''_{q,\Gamma}(k) \frac{h^{2q}}{(4r)^{2q+1}} \|\sigma\|_{C^{2q}}.$$

Here the coefficients $\{\alpha_l\}$ are given by (6.2), and $Q_q(\alpha_l)$ denotes the approximation of the coefficient integral of (6.2) by Gaussian quadrature with q points.

The theorem makes several assumptions that may not be true of the geometry discretization in its original form, notably the assumption that the placed disks do not intersect with other geometry, or the requirement that source panels supply sufficient quadrature resolution not just for themselves, but also for adjacent panels (which masquerades in Theorem 6.1 as the assumption of equal panel sizes). All these issues can be remedied by adequate refinement of the source geometry. An efficient, tree-based algorithm is available [79] to accomplish this.

To avoid quadratic scaling of the computational cost with the number of degrees of freedom, boundary integral equation methods require some form of acceleration, often through a variant of the Fast Multipole method (FMM [8]). In the context of QBX, it is convenient to exploit that the expansions produced as the output of the far-field stage of the FMM are the same ones employed by the quadrature method.

 However, without some care, loss of accuracy may occur [68]. We make use of the 'GIGAQBX' fast algorithm of [80] to obtain guaranteed accuracy at linearly scaling cost. This algorithm modifies the conventional FMM by forcing direct computation of interactions that may endanger the accuracy of the computed QBX expansion, in addition to a number of modifications to retain efficiency and linear scaling in that setting.

Another feature in GIGAQBX is the adaptive refinement activated when two or more source geometries get close to each other, causing near-singular evaluations of the boundary integral. The adaptive refinement is designed to continue until the expansion disks get out of the region of the source geometry [80]. Under the HADF, one might expect that many levels of refinement are needed when two particles are brought to near contact. However, the steric potential (2.16) also acts to prevent particles from getting too close to each other.

With the use of the short range repulsive potential, we found that the count of continuous refinements to be at most 3 to 5 levels at each time step for simulations presented in this work. Moreover, if the target point is geometrically on the wrong side (e.g. the interior region for the exterior problem), the GIGAQBX approximates analytic continuation of the potential across the boundary Γ , leading to benign behavior even in degenerate cases.

Our simulation codes make use of the software package 'Pytential' [40], which is in turn built upon FMMLIB [27] for some of its expansion and translation operator infrastructure.

7. Conclusions. Topological transitions of a lipid bilayer membrane, such as membrane fusion and fission, involve rearrangement of lipid molecules in the bilayer. Consequently the well-known Helfrich free energy requires modification to account for lipid granularity to resolve the detailed lipid re-modeling during membrane fusion or fission [61, 13, 72]. By using a modified Helfrich free energy with van der Waals repulsion and a hydrophobic potential for lipid tail-solvent interaction, Ryham et al. [72] calculated a least energy pathway of membrane fusion. Building on these results, the main motivation for the work presented here is to construct a hybrid continuum lipid model at the mesoscopic scales to capture both the lipid granularity and the long-range interaction during the self-assembly of lipid molecules and fusion/fission dynamics of a lipid bilayer membrane.

Our continuum coarse-grained model for lipids focuses on the hydrophobic interactions between lipid tails, and an SKIE formulation of the hydrophobic stress is derived and used for obtaining particle dynamics. We also show that the long-range hydrophobic attraction potential is non-pairwise, and thus requires special treatment within the coarse-grained model framework. The GIGAQBX scheme—an improved version of the QBX-FMM scheme with guaranteed accuracy—is used in the discretization, solver, and evaluation phases of the SKIE to achieve high accuracy and asymptotically optimal complexity. Simulation results of our model show that during the self-assembly process, coarse-grained lipid particles form structures (such as micelles and bilayers) that may further fuse together to form a single bilayer membrane. These results show that our approach can naturally capture the mesoscopic dynamics of membrane fusion/fission. Furthermore, we show that the hydrophobic interactions give rise to membrane curvature minimization, which is an indication of the origin of bending rigidity in a bilayer membrane.

It is straightforward to apply the numerical scheme developed in this paper to study particles of arbitrary shape. With slight algorithmic modification, the scheme can also accurately capture the collision dynamics that many researchers may regard as rather difficult to deal with.

We also illustrate that the lipid hydrodynamics under HADF gives rise to macroscopic mechanical properties of a lipid bilayer membrane that are consistent with other results in the literature. The flexibility of our hybrid approach allows us to consider a mixture of two lipid species and how spontaneous sorting (phase separation) of two lipid species leads to membrane fission, consistent with results from phase-field simulations [49]. Our future goal is to extend the current framework to three-dimensional lipid system. We will incorporate fluctuating hydrodynamics into the boundary integral formulation to extract physical properties of the lipid bilayer membrane such as membrane diffusivity, bending rigidity and the surface tension. By modification of the interfacial labels, HADF can account for charged lipids and study their impact on elastic properties of bilayer [20]. Since we have immersed the particles in a zero-Reynolds flow, it is possible to study the rheological properties of micelle networks in large particle simulations [50]. Finally, we also aim to investigate the continuum limit of our hybrid model and make comparison with functionalized Canham-Helfrich models.

Acknowledgments. Part of the work was performed when S.-P. Fu, S. Jiang, A. Klöckner, and M. Wala were participating the 2017 HKUST-ICERM workshop "Integral Equation Methods, Fast Algorithms and Their Applications to Fluid Dynamics and Materials Science." The authors thank the anonymous referees, Joshua Schrier, Jasun Gong, John Lowengrub and Jun Allard for valuable feedback. S. Jiang was supported by NSF under grants DMS-1418918 and DMS-1720405, and by the Flatiron Institute, a division of the Simons Foundation. A. Klöckner and M. Wala were supported in part by NSF under grants DMS-1418961 and DMS-1654756. Y.-N. Young was supported by NSF under grants DMS-1412789 and DMS-1614863.

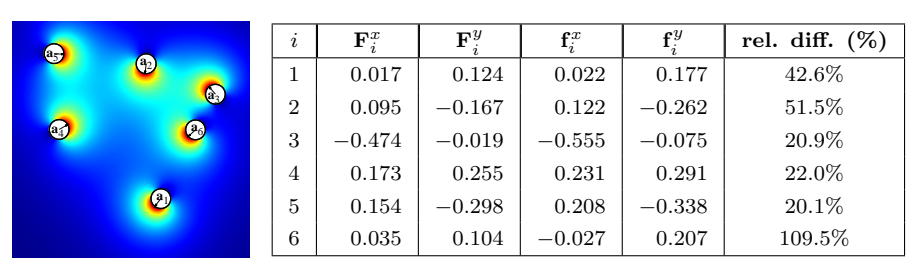


Fig. 10. The pseudo-color map shows a configuration of six, randomly placed particles with random orientations. The table (in pN) provides values for the x and y components of force $\mathbf{F}_i^{\{x,y\}}$ calculated from the HADF and the force $\mathbf{f}_i^{\{x,y\}}$ calculated assume a pairwise potential (A.1). The rightmost column shows the relative difference $\|\mathbf{F}_i - \mathbf{f}_i\|/\|\mathbf{F}_i\|$.

Appendix A. Pairwise potentials. We show that pairwise potentials do not closely approximate the HADF. Consider the case of N many particles in general position and orientation. Their associated pairwise potential is

679 (A.1)
$$\sum_{i=1}^{N} \sum_{j>i} \phi_{ij},$$

where ϕ_{ij} is the functional (1.1) evaluated on $\Omega = \mathbb{R}^2 \setminus (P_i \cup P_j)$. Differentiating (A.1) with respect to position \mathbf{a}_i yields the force

682 (A.2)
$$\mathbf{f}_i = \sum_{j \neq i} \mathbf{f}_{ij}, \quad \mathbf{f}_{ij} = -\nabla_{\mathbf{a}_i} \phi_{ij}.$$

That is, we calculate \mathbf{f}_{ij} using (2.2) for a fluid domain containing only two particles, P_i and P_j , and then sum the results for j = 1, ..., N, $j \neq i$. Finally, let Φ be the HADF for all N particles, and calculate the hydrophobic force $\mathbf{F}_i = -\nabla_{\mathbf{a}_i}\Phi$ using (2.2) over the fluid domain that contains all particles.

The table in Figure 10 compares the non-pairwise \mathbf{F}_i and pairwise \mathbf{f}_i forces for a sample particle configuration (Figure 10, pseudo-color map). The forces show significant differences for all six particles (Figure 10, rightmost column), suggesting that it is insufficient to use a pairwise potential to calculate HADF as formulated in the present work. We note, however, that owing to the form of the free-space Green's function (5.4), the correlations between particles decays like $\exp(-D/\rho)$ in their distance D. This makes it possible localize interaction to tens of particles by setting a cut-off radius in the layer potential evaluations.

695 REFERENCES

688

689

690

691

692

693

694

699 700

701

702

703

704

705

706

707

708

 $709 \\ 710$

711

712

713

 $714 \\ 715$

716

717

718

719

720

721

722

723

724

725

726

727

- [1] C. BANDLE AND A. WAGNER, Second domain variation for problems with robin boundary
 conditions, Journal of Optimization Theory and Applications, 167 (2015), pp. 430–463,
 https://doi.org/10.1007/s10957-015-0801-1.
 - [2] BARTELS, SÖREN, DOLZMANN, GEORG, AND NOCHETTO, RICARDO H., A finite element scheme for the evolution of orientational order in fluid membranes, ESAIM: M2AN, 44 (2010), pp. 1–31, https://doi.org/10.1051/m2an/2009040.
 - [3] D. BOAL, Mechanics of the Cell Second Edition, Cambridge University Press, Cambridge, United Kingdom, 2012.
 - [4] J. F. Brady and G. Bossis, Stokesian dynamics, Annual Review of Fluid Mechanics, 20 (1988), pp. 111–157, https://doi.org/10.1146/annurev.fl.20.010188.000551.
 - [5] H. BRAKHAGE AND P. WERNER, Über das Dirichletsche Auβenraumproblem für die Helmholtzsche Schwingungsgleichung, Archiv der Mathematik, 16 (1965), pp. 325–329, https://doi.org/10.1007/BF01220037.
 - [6] S. Burger, T. Fraunholz, C. Leirer, R. H. W. Hoppe, A. Wixforth, M. A. Peter, and T. Franke, Comparative study of the dynamics of lipid membrane phase decomposition in experiment and simulation, Langmuir, 29 (2013), pp. 7565–7570, https://doi.org/10.1021/ la401145t.
 - [7] A. J. Burton and G. F. Miller, The application of integral equation methods to the numerical solution of some exterior boundary-value problems. a discussion on numerical analysis of partial differential equations, Proceedings of the Royal Society Londo A, 323 (1971), pp. 201–210.
 - [8] J. CARRIER, L. GREENGARD, AND V. ROKHLIN, A fast adaptive multipole algorithm for particle simulations, SIAM J. Sci. Statist. Comput., 9 (1988), pp. 669–686, https://doi.org/10. 1137/0909044.
 - [9] P. CHLANDA, E. MEKHEDOV, H. WATERS, C. L. SCHWARTZ, E. R. FISCHER, R. J. RYHAM, F. S. COHEN, P. S. BLANK, AND J. ZIMMERBERG, The hemifusion structure induced by influenza virus haemagglutinin is determined by physical properties of the target membranes, Nature Microbiology, 1 (2016), p. 16050.
 - [10] F.-X. CONTRERAS, L. SÁNCHEZ-MAGRANER, A. ALONSO, AND F. M. GOÑI, Transbilayer (flip-flop) lipid motion and lipid scrambling in membranes, FEBS Letters, 584 (2010), pp. 1779 1786, https://doi.org/10.1016/j.febslet.2009.12.049. Frontiers in Membrane Biochemistry.
 - [11] I. R. COOKE AND M. DESERNO, Solvent-free model for self-assembling fluid bilayer membranes: Stabilization of the fluid phase based on broad attractive tail potentials, The Journal of Chemical Physics, 123 (2005), p. 224710, https://doi.org/10.1063/1.2135785.
- 730 [12] S. DAI AND K. PROMISLOW, Geometric evolution of bilayers under the functionalized 731 Cahn-Hilliard equation, Proc. Roy. Soc. A, 469 (2013), p. 20120505.

- [13] S. Dai and K. Promislow, Competitive geometric evolution of amphiphilic interfaces, SIAM.
 J. Math. Anal., 47 (2015), pp. 347–380.
- 734 [14] D. E. DISCHER AND A. EISENBERG, Polymer vesicles, Science, 297 (2002), pp. 967–973.

742

743

744745

746

747

748

 $749 \\ 750$

751

752

753

754

756

757

758

759

760

 $761 \\ 762$

763

764

 $765 \\ 766$

767

768 769

770

771

772

 $773 \\ 774$

775

779

780

781

782

783

784

- 735 [15] W. A. DUCKER AND D. MASTROPIETRO, Forces between extended hydrophobic solids: Is there a long-range hydrophobic force?, Current Opinion in Colloid & Interface Science, 22 (2016), pp. 51 58, https://doi.org/10.1016/j.cocis.2016.02.006.
- 738 [16] C. L. EPSTEIN, L. GREENGARD, AND A. KLÖCKNER, On the convergence of local expansions 739 of layer potentials, SIAM J. Numer. Anal., 51 (2013), pp. 2660–2679, https://doi.org/10. 740 1137/120902859.
 - [17] J. C. ERIKSSON, S. LJUNGGREN, AND P. M. CLAESSON, A phenomenological theory of long-range hydrophobic attraction forces based on a square-gradient variational approach, J. Chem. Soc., Faraday Trans. 2, 85 (1989), pp. 163–176, https://doi.org/10.1039/F29898500163.
 - [18] E. EVANS, V. HEINRICH, F. LUDWIG, AND W. RAWICZ, Dynamic tension spectroscopy and strength of biomembranes, Biophysical Journal, 85 (2003), pp. 2342 – 2350, https://doi. org/10.1016/S0006-3495(03)74658-X.
 - [19] L. C. EVANS, Partial Differential Equations, vol. 19 of Graduate Studies in Mathematics, AMS, Providence, RI, 2001.
 - [20] H. A. FAIZI, S. L. FREY, J. STEINKÜLER, R. DIMOVA, AND P. M. VLAHOVSKA, Bending rigidity of charged lipid bilayer membranes, Soft Matter, (2019), p. Advance Article.
 - [21] W. Feng, Z. Guan, J. Lowengrub, C. Wang, S. Wise, and Y. Chen, A uniquely solvable, energy stable numerical scheme for the functionalized Cahn-Hilliard equation and its convergence analysis, J. Sci. Comput., 76 (2018), pp. 1938–1967.
 - [22] C. François-Martin, J. E. Rothman, and F. Pincet, Low energy cost for optimal speed and control of membrane fusion, Proceedings of the National Academy of Sciences, (2017), https://doi.org/10.1073/pnas.1621309114.
 - [23] S.-P. Fu, Z. Peng, H. Yuan, R. Kfoury, and Y.-N. Young, Lennard-jones type pair-potential method for coarse-grained lipid bilayer membrane simulations in lammps, Computer Physics Communications, 210 (2017), pp. 193–203, https://doi.org/10.1016/j.cpc. 2016.09.018.
 - [24] A. J. GARCÍA-SÁEZ, S. CHIANTIA, AND P. SCHWILLE, Effect of line tension on the lateral organization of lipid membranes, Journal of Biological Chemistry, 282 (2007), pp. 33537– 33544, https://doi.org/10.1074/jbc.M706162200.
 - [25] P. GERA AND D. SALAC, Cahn-Hilliard on surfaces: A numerical study, Applied Mathematics Letters, 73 (2017), pp. 56 61, https://doi.org/https://doi.org/10.1016/j.aml.2017.02.021.
 - [26] D. GILBARG AND N. S. TRUDINGER, Elliptic Partial Differential Equations of Second Order, Springer, Mar. 2015.
 - [27] Z. GIMBUTAS AND L. GREENGARD, Fmmlib2d, https://github.com/zgimbutas/fmmlib2d. Accessed June 2018.
 - [28] G. Gompper and M. Schick, Correlation between structural and interfacial properties of amphiphilic systems, Phys. Rev. Lett., 65 (1990), pp. 1116–1119.
 - [29] A. GREENBAUM, L. GREENGARD, AND G. B. McFADDEN, Laplace's equation and the Dirichlet-Neumann map in multiply connected domains, J. Comput. Phys., 105 (1993), pp. 267–278.
 - [30] L. GREENGARD, M. C. KROPINSKI, AND A. MAYO, Integral equation methods for Stokes flow and isotropic elasticity in the plane, J. Comput. Phys., 125 (1996), pp. 403–414.
- [31] L. Greengard and V. Rokhlin, A fast algorithm for particle simulations, J. Comput. Phys.,
 777 73 (1987), pp. 325–348.
 [32] L. F. Greengard and J. Huang, A new version of the fast multipole method for screened
 - [32] L. F. GREENGARD AND J. HUANG, A new version of the fast multipole method for screened coulomb interactions in three dimensions, J. Comput. Phys., 180 (2002), pp. 642–658.
 - [33] W. HELFRICH, Elastic properties of lipid bilayers: theory and possible experiments, Z. Naturforsch. C, 28 (1973), pp. 693-703.
 - [34] J. Hu, Y. Shibata, C. Voss, T. Shemesh, Z. Li, M. Coughlin, M. M. Kozlov, T. A. Rapoport, and W. A. Prinz, Membrane proteins of the endoplasmic reticulum induce high-curvature tubules, Science, 319 (2008), pp. 1247–1250, https://doi.org/10.1126/ science.1153634.
- 786 [35] J. N. ISRAELACHVILI, S. MARČELJA, AND R. G. HORN, Physical principles of membrane organi-787 zation, Quarterly Reviews of Biophysics, 13 (1980), p. 121–200, https://doi.org/10.1017/ 788 S0033583500001645.
- 789 [36] S. JIANG, M. RACHH, AND Y. XIANG, An efficient high order method for dislocation climb in two dimensions, SIAM J. Multiscle Model. Simul., 15 (2017), pp. 235–253.
- [37] M. JURÁSEK AND R. VÁCHA, Self-assembled clusters of patchy rod-like molecules, Soft Matter,
 13 (2017), pp. 7492-7497, https://doi.org/10.1039/C7SM01384A.
- 793 [38] I. Kabelka and R. Vácha, Optimal hydrophobicity and reorientation of amphiphilic peptides

- 794 translocating through membrane, Biophysical Journal, 115 (2018), pp. 1045 - 1054, https: 795 //doi.org/https://doi.org/10.1016/j.bpj.2018.08.012. 796
 - [39] A. KLÖCKNER, A. BARNETT, L. GREENGARD, AND M. O'NEIL, Quadrature by expansion: A new method for the evaluation of layer potentials, J. Comput. Phys., 252 (2013), pp. 332–349.
- 798 [40] A. KLÖCKNER AND M. WALA, Pytential: a software package for the evaluation of layer poten-799 tials, https://github.com/inducer/pytential. Accessed June 2018.
 - [41] D. I. KOPELEVICH AND J. F. NAGLE, Correlation between length and tilt of lipid tails, The Journal of Chemical Physics, 143 (2015), p. 154702, https://doi.org/10.1063/1.4932971.
 - M. M. Kozlov, Determination of Lipid Spontaneous Curvature From X-Ray Examinations of Inverted Hexagonal Phases, Humana Press, Totowa, NJ, 2007, pp. 355–366.
 - [43] N. Kraitzman and K. Promislow, Pearling bifucations in the strong functionalized Cahn-Hilliard free energy, SIAM J. Math. Anal., 50 (2018), pp. 3395-3426.
 - [44] R. Kress, Linear Integral Equations, Applied Mathematical Sciences, Springer New York, 2014.
 - [45] P. I. Kuzmin, S. A. Akimov, Y. A. Chizmadzhev, J. Zimmerberg, and F. S. Cohen, Line tension and interaction energies of membrane rafts calculated from lipid splay and tilt, Biophysical Journal, 88 (2005), pp. 1120 - 1133, https://doi.org/10.1529/biophysj.104. 048223.
 - [46] P. LAX, Functional analysis, Pure and applied mathematics, Wiley, 2002.

800

801 802

803

804

805

806

807 808

809

810

811

812 813

814 815

816

817

818 819

820 821

822

823

824

825 826

827

828 829

830 831

832

833

834

841

842

843 844

845

846

847

- [47] L. G. Leal, Advanced Transport Phenomena: Fluid Mechanics and Convective Transport Processes, Cambridge Series in Chemical Engineering, Cambridge University Press, 2007, https://doi.org/10.1017/CBO9780511800245.
- [48] Q. Lin, E. E. Meyer, M. Tadmor, J. N. Israelachvili, and T. L. Kuhl, Measurement of the long- and short-range hydrophobic attraction between surfactant-coated surfaces, Langmuir, 21 (2005), pp. 251–255, https://doi.org/10.1021/la048317q. PMID: 15620310.
- [49] J. S. LOWENGRUB, A. RATZ, AND A. VOIGT, Phase-field modeling of the dynamics of multicomponent vesicles: Spinodal decomposition, coarsening, budding, and fission, Phys. Rev. E, 79 (2009), p. 031926.
- [50] V. Lutz-Bueno, R. Pasquino, M. Liebi, J. Kohlbrecher, and P. Fischer, "viscoelasticity enhancement of surfactant solutions depends on molecular conformation: influence of surfactant headgroup structure and its counterion, Langmuir, 32 (2016), pp. 4239–4250.
- [51] J. L. MACCALLUM AND D. P. TIELEMAN, Hydrophobicity scales: a thermodynamic looking glass into lipid-protein interactions, Trends Biochem. Sci., 36 (2011), pp. 653-662.
- [52] S. J. Marrink, H. J. Risselada, S. Yefimov, D. P. Tieleman, and A. H. de Vries, The martini force field: Coarse grained model for biomolecular simulatons, The Journal of Physical Chemistry B, 111 (2007), pp. 7812–7824.
- [53] L. I. Menshikov, P. L. Menshikov, and P. O. Fedichev, Phenomenological model of hydrophobic and hydrophilic interactions, Journal of Experimental and Theoretical Physics, 125 (2017), pp. 1173–1188, https://doi.org/10.1134/S1063776117120056.
- [54] E. E. MEYER, K. J. ROSENBERG, AND J. ISRAELACHVILI, Recent progress in understanding hydrophobic interactions, Proceedings of the National Academy of Sciences, 103 (2006), pp. 15739-15746, https://doi.org/10.1073/pnas.0606422103.
- 835 [55] M. MIKUCKI AND Y. ZHOU, Curvature-driven molecular flow on membrane surface, SIAM 836 Journal on Applied Mathematics, 77 (2017), pp. 1587–1605, https://doi.org/10.1137/ 837 16M1076551.
- 838 [56] J. F. NAGLE, Experimentally determined tilt and bending moduli of single-component lipid 839 bilayers, Chemistry and Physics of Lipids, 205 (2017), pp. 18 – 24. 840
 - [57] J. F. NAGLE, Mechanical properties of lipid bilayers, European Pharmaceutical Journal, 64 (2017), pp. 22 - 23.
 - [58] J. F. NAGLE, M. S. JABLIN, S. TRISTRAM-NAGLE, AND K. AKABORI, What are the true values of the bending modulus of simple lipid bilayers?, Chemistry and Physics of Lipids, 185 (2015), pp. 3 – 10, https://doi.org/10.1016/j.chemphyslip.2014.04.003. Membrane mechanochemistry: From the molecular to the cellular scale.
 - [59] J. C. Nédélec, Acoustic and Electromagnetic Equations: Integral Representations for Harmonic Problems, vol. 144 of Applied Mathematical Sciences, Springer, New York, 2001.
- [60] H. NOGUCHI, Solvent-free coarse-grained lipid model for large-scale simulations, The Journal 848 849 of Chemical Physics, 134 (2011), p. 055101, https://doi.org/10.1063/1.3541246.
 - T. Ohta and K. Kawasaki, Equilibrium morphology of block copolymer melts, Macromolecules, 19 (1986), pp. 2621–2632, https://doi.org/10.1021/ma00164a028.
- 851 852 [62] F. W. J. Olver, N. I. O. S. (U.S.), and Technology, NIST Handbook of Mathematical 853 Functions, Cambridge University Press, May 2010, http://dlmf.nist.gov.
- [63] V. Parsegian and R. Rand, Chapter 13 interaction in membrane assemblies, in Struc-854 855 ture and Dynamics of Membranes, R. Lipowsky and E. Sackmann, eds., vol. 1 of Hand-

- 856 book of Biological Physics, North-Holland, 1995, pp. 643 690, https://doi.org/10.1016/857 S1383-8121(06)80006-0.
- [64] V. A. Parsegian and B. W. Ninham, Temperature-dependent van der waals forces, Biophys.
 J., 10 (1970), pp. 664-674.
- 860 [65] A. D. Petelska, Interfacial tension of bilayer lipid membranes, Central European Journal of Chemistry, 10 (2012), pp. 16–26, https://doi.org/10.2478/s11532-011-0130-7.
- 862 [66] S. PLIMPTON, P. CROZIER, AND A. THOMPSON, Lammps-large-scale atomic/molecular mas-863 sively parallel simulator, Sandia National Laboratories, 18 (2007), p. 43.

865 866

867

868

 $869 \\ 870$

871

872

 $873 \\ 874$

875

876 877

878

879

880

882

883

884

885

886

887 888

889

890

891

892

893

- [67] M. RACHH, Integral equation methods for problems in electrostatics, elastostatics and viscous flow, PhD thesis, New York University, 5 2015.
- [68] M. RACHH, A. KLÖCKNER, AND M. O'NEIL, Fast algorithms for Quadrature by Expansion I: Globally valid expansions, Journal of Computational Physics, 345 (2017), pp. 706–731, https://doi.org/10.1016/j.jcp.2017.04.062.
 - [69] B. Ren, A. Ruditskiy, J. H. K. Song, and I. Kretzschmar, Assembly behavior of iron oxide-capped janus particles in a magnetic field, Langmuir, 28 (2012), pp. 1149–1156, https://doi.org/10.1021/la203969f. PMID: 22149478.
- [70] E. RIDEAU, R. DIMOVA, P. SCHWILLE, F. R. WURM, AND K. LANDFESTER, Liposomes and polymersomes: a comparative review towards cell mimicking, Chem. Soc. Rev., (2018), pp. –, https://doi.org/10.1039/C8CS00162F.
- [71] B. ROZYCKI AND R. LIPOWSKY, Spontaneous curvature of bilayer membranes from molecular simulations: Asymmetric lipid densities and asymmetric adsorption, The Journal of Chemical Physics, 142 (2015), p. 054101, https://doi.org/10.1063/1.4906149.
- [72] R. J. RYHAM, T. S. KLOTZ, L. YAO, AND F. S. COHEN, Calculating transition energy barriers and characterizing activation states for steps of fusion, Biophys. J., 110 (2016), pp. 1110– 1124.
- 881 [73] M. Schiffer, Variation of domain functionals, Bull. Amer. Math. Soc., 60 (1954), pp. 303–328.
 - [74] B. SEGUIN AND E. FRIED, Calculating the bending moduli of the Canham-Helfrich free-energy density, Journal of Mathematical Biology, 68 (2014), pp. 345–361.
 - [75] B. SEGUIN AND E. FRIED, Microphysical derivation of the Canham-Helfrich free-energy density, vol. 137, Springer Proceedings in Mathematics & Statistics, 2015, pp. 647—665.
 - [76] M. M. TERZI AND M. DESERNO, Novel tilt-curvature coupling in lipid membranes, The Journal of Chemical Physics, 147 (2017), p. 084702, https://doi.org/10.1063/1.4990404.
 - [77] M. M. TERZI AND M. DESERNO, Lipid Membranes: From Self-assembly to Elasticity, Springer International Publishing, Cham, 2018, pp. 105–166, https://doi.org/10.1007/ 978-3-319-56348-0_3.
 - [78] R. M. VENABLE, F. L. BROWN, AND R. W. PASTOR, Mechanical properties of lipid bilayers from molecular dynamics simulation, Chemistry and Physics of Lipids, 192 (2015), pp. 60 – 74, https://doi.org/10.1016/j.chemphyslip.2015.07.014. ORNL workshop on Biomembranes.
 - [79] M. WALA AND A. KLÖCKNER, A Fast Algorithm for Quadrature by Expansion in Three Dimensions, ArXiv e-prints, (2018), https://arxiv.org/abs/1805.06106.
- [80] M. Wala and A. Klöckner, A fast algorithm with error bounds for quadrature by expansion,
 Journal of Computational Physics, 374 (2018), pp. 135 162, https://doi.org/10.1016/j.
 jcp.2018.05.006.
- 899 [81] Y. Wang, J. K. Sigurdsson, E. Brandt, and P. Atzberger, Dynamic implicit-solvent 900 coarse-grained models of lipid bilayer membranes: Fluctuating hydrodynamics thermostat, 901 Phys. Rev. E, 88 (2013), p. 023301.
- 902 [82] J. Yoo, M. B. Jackson, and Q. Cui, A comparison of coarse-grained and continuum models 903 for membrane bending in lipid bilayer fusion pores, Biophysical Journal, 104 (2013), pp. 841 904 - 852.

Supplementary Material

Simulation of Multiscale Hydrophobic Lipid Dynamics via Efficient Integral Equation Methods Szu-Pei P. Fu^{1,*}, Rolf J. Ryham¹, Andreas Klöckner², Matt Wala², Shidong Jiang³, Y.-N. Young³,

⁹ Fordham University, Department of Mathematics, Bronx, NY, USA

²Department of Computer Science, University of Illinois at Urbana-Champaign, Urbana-

11 bana, IL 61801 USA

³Department of Mathematical Sciences, New Jersey Institute of Technology, Newark,

13 NJ 07102 USA

*Corresponding author. Address: Fordham University, Department of Mathematics, 441 E. Fordham Rd, Bronx, NY 10458. email: sfu17@fordham.edu

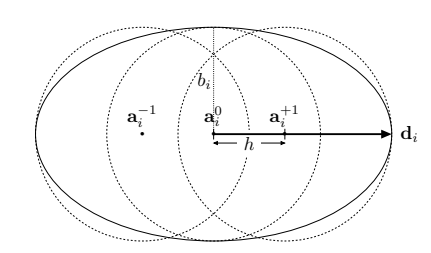


Fig. S1. Schematic of elliptical repulsion.

S1. Elliptical Excluded Volume Repulsion. For any elliptical particle with semi-major axis a_i and semi-minor axis b_i , the rigid body repulsion is designed as follows. Consider three circle centers $\mathbf{a}_i^k = \mathbf{a}_i + kh\mathbf{d}_i$, $h = (a_i - b_i), k \in \{-1, 0, +1\}$ with radii b_i (Figure S1) and use (2.16) with c_0 divided by 3 to calculate the forces $\mathbf{f}_i^k, k \in \{-1, 0, +1\}$ and torque τ_i^{-1} and τ_i^{+1} . For two elliptical particles, the total interactions are given by

$$\mathbf{f}_{ij}^{kl} = \frac{c_0}{3} \frac{q}{(|\mathbf{a}_i^k - \mathbf{a}_j^l| - (b_i + b_j))^{q+1}} \frac{\mathbf{a}_i^k - \mathbf{a}_j^l}{|\mathbf{a}_i^k - \mathbf{a}_j^l|}, \quad i \neq j, \quad k, l \in \{-1, 0, +1\},$$

$$\mathbf{F}_i^{\text{rep}} = \sum_{\substack{j=1\\j \neq i}}^{N} \sum_{k,l} \mathbf{f}_{ij}^{kl}, \quad k, l \in \{-1, 0, +1\},$$

$$\tau_i^{\text{rep}} = \sum_{\substack{j=1\\j \neq i}}^{N} \sum_{k} h(\mathbf{f}_{ij}^{-1k} - \mathbf{f}_{ij}^{+1k}) \times \mathbf{d}_i, \quad k \in \{-1, 0, +1\}.$$

24 The total repulsive potential is

17

18

19

21

27

$$\Phi_i^{\text{rep}} = \frac{1}{2} \sum_{\substack{j=1\\j \neq i}}^N \sum_k \frac{c_0}{3} \frac{1}{(|\mathbf{a}_i^k - \mathbf{a}_j^l| - (b_i + b_j))^q}, \quad k \in \{-1, 0, +1\}.$$

26 The total repulsive force is identical to (2.16) whenever particles are circular.

S2. Numerical Validations.

S2.1. Force and Torque Relations. We validate formulas (2.2, 2.3) by centered difference approximation. Following (2.10),

(S1)
$$\mathbf{v} \cdot \mathbf{F}_{i} = -\frac{d}{d\epsilon} \Phi(\mathbf{a}_{i} + \epsilon \mathbf{v}, \theta_{i})|_{\epsilon=0} \approx -\frac{\Phi(\mathbf{a}_{i} + \epsilon \mathbf{v}, \theta_{i}) - \Phi(\mathbf{a}_{i} - \epsilon \mathbf{v}, \theta_{i})}{2\epsilon},$$
$$\omega \tau_{i} = -\frac{d}{d\epsilon} \Phi(\mathbf{a}_{i}, \theta_{i} + \omega \epsilon)|_{\epsilon=0} \approx -\frac{\Phi(\mathbf{a}_{i}, \theta_{i} + \omega \epsilon) - \Phi(\mathbf{a}_{i}, \theta_{i} - \omega \epsilon)}{2\epsilon},$$

where i = 1, ..., N. We write $\Phi(\mathbf{a}_i, \theta_i)$ in place of $\Phi(\Omega, f)$ to emphasize that for the moment variations are taken with respect to the *i*th particle, while keeping the others particles fixed. For the three-particle setup from Figure 1A and step size $\epsilon = 0.05$, we get the following values:

	Centered Difference	ence	Variations $(2.2-2.3)$		
	\mathbf{F}_i	$ au_i$	\mathbf{F}_i	$ au_i$	
35	$\langle -0.94496, +1.37954 \rangle$	+0.90685	$\langle -0.83884, +1.35038 \rangle$	+0.92534	
	$\langle -0.28603, -0.46196 \rangle$	+0.02815	$\langle -0.26879, -0.43257 \rangle$	+0.02923	
	$\langle +1.17189, -0.90103 \rangle$	-0.23972	$\langle +1.20538, -0.91928 \rangle$	-0.23962	

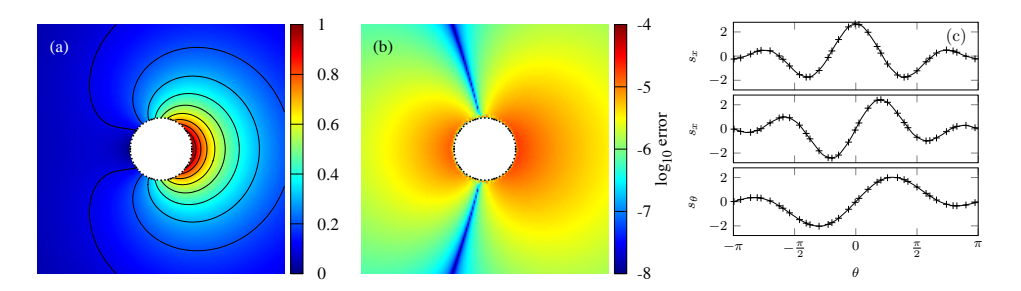


Fig. S2. Single Janus particle simulation ($\rho=4a$): (a) Surface-contour plot of the action field solution u. The points along the boundary (circle) show the distribution of panels and Gauss-Legendre points. (b) Error plot (in logarithmic scale) for the BIE-QBX-FMM solution and analytical solution S2. (c) From top to bottom: normal and tangential stresses calculated by BIE-QBX-FMM (+ symbols) and their corresponding analytical values (solid curves).

The agreement between the centered difference approximation and the variational derivatives supports (2.2-2.3).

S2.2. Single Particle Validation. One can analytically solve the exterior problem (1.3) for a single two-dimensional disk with boundary condition (2.14) using the free-space Green's function (5.4);

41 (S2)
$$u(r,\theta) = \frac{1}{2} \left(\frac{K_0\left(\frac{r}{\rho}\right)}{K_0\left(\frac{a}{\rho}\right)} + \frac{K_1\left(\frac{r}{\rho}\right)}{K_1\left(\frac{a}{\rho}\right)} \cos\left(\theta\right) \right).$$

Here (r, θ) are polar coordinates relative to the particle center (the origin), $\mathbf{d}_1 = \langle 1, 0 \rangle$ is the particle orientation, and a and $\rho = 4a$ are the disk radius and decay length, respectively.

Figure S2(a) shows of the action field contours for (S2). Consistent with the boundary condition (2.14), the hydrophobic attraction is strongest in the neighborhood of the right semicircle. The smooth boundary data results in the hydrophobic attraction extending weakly to the left of the particle. The size of the contours are proportional to the decay length ρ , e.g. the farthest contour $u(r, \theta) = 0.1$ in Figure S2(a) would grow for larger ρ .

Figure S2(b) shows the corresponding relative errors of the BIE-QBX-FMM with $N_{\text{bdy}} = 70$ boundary points and QBX order p = 6. The reflectional symmetry of the error distribution is due to the symmetric particle shape and boundary condition. The numerically computed interfacial stresses (e.g. gradients in the action field) are also in excellent agreement with their analytical values. In Figure S2(c), the + markers are for the numerically calculated pointwise normal and tangential stress densities,

(S3)
$$\langle s_x(\theta), s_y(\theta) \rangle = \mathbf{T}(a, \theta) \cdot \mathbf{i}_r, \quad s_{\theta}(\theta) = \mathbf{i}_r \times (\mathbf{T}(a, \theta) \cdot \mathbf{i}_r),$$

respectively, along the particle boundary. The smooth curves Figure S2(c) are the analytical values, obtained by plugging (S2) into the integrands of the equations (2.9). Thus the BIE-QBX-FMM yields a numerical solution that is highly accurate both in terms of the action field and its gradients along the domain boundary. From a physical perspective, an isolated particle has zero net force and torque (see (2.13)). Indeed, the integrals of force and torque curves in Figure S2(c) are all zero to about eight digit accuracy.

TABLE 1

Convergence tests as the QBX order p and number panels per particle $N_{\rm pan}$ vary. The number of Gauss-Legendre points $N_{\rm GL}=6$ per panel (yielding $N_{\rm bdy}=N_{\rm GL}N_{\rm pan}$ points per particle), FMM order $p_{FMM}=10$, GMRES tolerance tol_{GMRES} = 10^{-13} and 5×5 computational domain are fixed. $N_{\rm iter}$ is the number of iterations in GMRES.

		QBX order $p = 4$		QBX order $p = 6$		QBX order $p = 8$	
N_{pan}	$N_{ m bdy}$	$N_{ m iter}$	l_{∞} error	$N_{ m iter}$	l_{∞} error	$N_{ m iter}$	l_{∞} error
10	70	8	3.20×10^{-4}	8	2.01×10^{-5}	8	1.23×10^{-6}
20	140	8	2.00×10^{-5}	7	3.93×10^{-7}	7	1.23×10^{-8}
40	280	7	9.12×10^{-7}	8	2.21×10^{-7}	8	2.84×10^{-7}
80	560	8	5.96×10^{-8}	9	4.77×10^{-8}	8	5.01×10^{-8}

Continuing with the single particle test, Table 1 provides three sets of convergence tests where we tune the QBX parameters. The purpose of these tests is to acquire a suitable parameter set for efficient simulations. We fix the GMRES iterative scheme tolerance $tol_{\rm GMRES}=10^{-13}$ and use the FMM to expedite the matrix-vector multiplications in GMRES iterations. We divide each particle boundary into $N_{\rm pan}$ panels and fill in $N_{\rm GL}$ Gauss-Legendre points in each panel. This yields a total number of boundary points $N_{\rm bdy}=N_{\rm GL}N_{\rm pan}$. In the l_{∞} error columns, we compute the errors with respect to the analytical solution (S2) over a 5 × 5 computational domain sampling at 200 × 200 cartesian grid points (the error excludes the values inside the particle). Through our setting of the underlying fast multipole order $p_{FMM}=10$, the approximation of the layer potential has about eight digit accuracy, leading to the observed errors 'bottoming out' around that accuracy. As a result, the results for order p=10 are only marginally better than for the p=8 column, but require significantly more computational time.

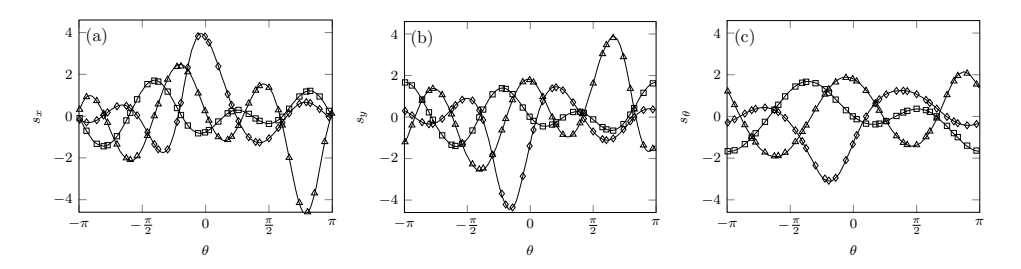


Fig. S3. Panels (a) and (b) show the normal stresses s_x and s_y , and panel (c) is for the tangential stress s_θ S3. The symbols are: \diamond -diamond for particle 1, \square -square for particle 2 and \triangle -triangle for particle 3. Net force and torque is zero 2.13 and so the integrals of the curves in panel (a) sum to zero. The same holds for panel (b) and for panel (c).

S2.3. Dissipative System with Constant Drag Coefficients. As an alternative numerical scheme, the metastable final states of self-assembly particles are achievable by using constant drag coefficients to update particle dynamics. The updated particle dynamics of centers $\mathbf{a}_i \in \mathbb{R}^2$ and orientations $\theta_i \in \mathbb{R}$ at $t = n\Delta t$ are given by

$$\mathbf{a}_{i}^{n+1} = \mathbf{a}_{i}^{n} + \frac{1}{\xi_{x}} \left(\mathbf{F}_{i} + \sum_{i \neq i} \mathbf{F}_{ij}^{\text{rep}} \right) \Delta t, \quad \theta_{i}^{n+1} = \theta_{i}^{n} + \frac{1}{\xi_{\theta}} \tau_{i} \Delta t.$$

86

87

89

90

91

92

94

95 96

97

98

99

100

101 102

103

104

105

106 107

108

109

110

111

112

113

114

115116

117

118

119120

To discretize (S4), we adopt the forward Euler scheme for configuration updates. We observe numerically, and use the values $\xi_{\mathbf{x}} = 4\pi\mu a$ and $\xi_{\theta} = 4\pi\mu a^3$ for an isolated circular particle of radius a and $\mu = 1$ cP for water viscosity. The numerical scheme for simulating dissipative system using proposed constant drag law is included in Algorithm 5.1.

This numerical test is to investigate a rough approximation of constant drag coefficients $\xi_{\mathbf{x}}$ and ξ_{θ} . We first place two circular particles on the same horizontal axis, with centers $\mathbf{a}_1 = \langle -2.5, 0 \rangle$ and $\mathbf{a}_2 = \langle 2.5, 0 \rangle$, and orientations $\theta_1 = 45^{\circ}$ and $\theta_2 = 135^{\circ}$ (The schematic is in Figure S4A). From the theory of HADF, the particle pair will move toward each other and rotate until the system energy reaches a minimum. Due to the effect of excluded volume repulsion, with the choice of $c_0 = 0.0166$ pN nm⁴, an equilibrium distance r_{12} between two particles can be measured. Three sets of simulations are performed: (1) Obtaining particle dynamics by solving a mobility problem; (2) Calculating dissipative dynamics using three dimensional translational and rotational drag coefficients $\xi_{\mathbf{x}} = 6\pi\eta a$ and $\xi_{\mathbf{x}} = 8\pi\eta a^3$ and (3) Calculating dissipative dynamics using translational and rotational drag coefficients $\xi_{\mathbf{x}} = 4\pi \eta a$ and $\xi_{\mathbf{x}} = 4\pi \eta a^3$. Both Figure S4B and Figure S4C show that the dynamics obtained from case (2) have much lower initiative translational and rotational velocity. Case (3) gives a very good agreement in dynamics for the first few nanoseconds. To explain this finding, from Stokesian dynamics, the resistance tensor is a function of particle pair-distances and the particle resistance will be a factor of $\log(r_{ij})$ in two dimensions. This observation shows that with a specific choice of constant drag coefficients the dynamics of many-body system may have very similar starting transition in selfassembly.

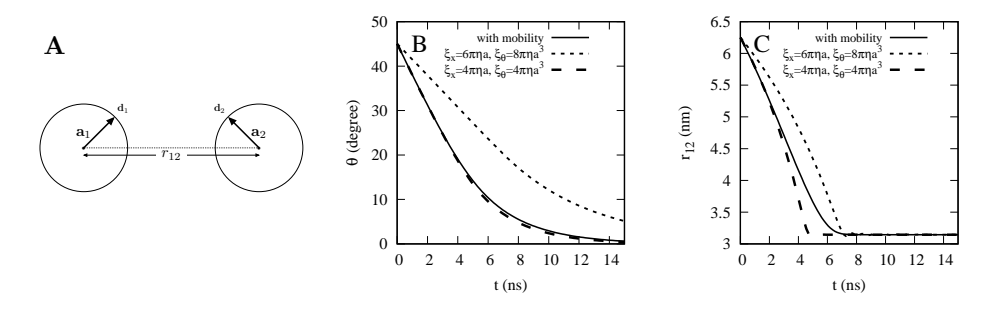


Fig. S4. Panel A: Schematic of two-particle simulations; Panel B: Plot of particle 2 orientations over time in three cases; Panel C: Plot of distance r_{12} over time in three cases.

S2.4. Multiple Particle Cases. For three-particle dynamics, there is no closed-form solution to compare with, and so we use a piecewise linear FEM to perform the numerical validations. The three particle configuration is the same as in 1(a), with centers $\mathbf{a}_1 = \langle -1, 0 \rangle$, $\mathbf{a}_2 = \langle 1.5, 3.3 \rangle$ and $\mathbf{a}_3 = \langle 1.5, -1.5 \rangle$, and orientations $\theta_1 = 18^\circ$, $\theta_2 = 240^\circ$ and $\theta_3 = -60^\circ$. In the FEM solution of (2.14, 1.3), we truncate the unbounded exterior domain Ω to the box $(-20, 20) \times (-20, 20) \subset \mathbb{R}^2$ and apply a homogeneous Dirichlet condition on the box boundary (5.1). To achieve an accuracy comparable to that of the BIE-QBX-FMM (Table 1), the FEM uses $N_{\rm bdy} = 250$ equally spaced points per particle boundary and a triangular mesh with roughly 15,000 points to discretize a truncated domain in Ω .

Figure S3(a)–(c) compares interfacial stresses (S3) derived by BIE-QBX-FMM (empty symbols) and the FEM (solid curves). The excellent agreement between the

results suggests that the integral equation method and the finite element method with appropriate truncation do an equally good job of calculating the interfacial stresses, and in practice would yield indistinguishable dynamics. The BIE-QBX-FMM, however, has the advantages that it uses far fewer mesh points than the FEM to achieve the same accuracy, and that it is straightforward to discretize boundaries of moving particles using high-order quadratures. In contrast, in the FEM each change in particle configuration involves the generation of a new triangular mesh as well as the artificial truncation of the domain, leading to much higher computational cost to achieve the same accuracy.

Table 2 Timing results for $N = \{250, 500, 1000, 2000\}$ particles with $N_{\rm bdy} = 70$ boundary points per particle and $tol_{\rm GMRES} = 10^{-5}$.

$N_{ m particle}$	$N_{ m bdy}$	L_x	L_y	Iter.	$T_{ m GMRES}/T_{ m total}$	$T_{ m total}/T_{ m ref}$
250	17500	100	100	32	0.67938	9.7
500	35000	200	200	28	0.66299	14.4
1000	70000	200	200	32	0.70062	32.4
2000	140000	400	400	31	0.64738	55.3

S2.5. Large Collection Simulations. The simulation in Figure 7 used N=25 particles and this number was sufficient for particles to self-assemble into a vesicle shape. In realistic applications though, such as membrane fusion or vesicle deformations, the problem is three-dimensional and the number of Janus-type particles involved would be much larger, on the order of thousands to tens of thousands. Thus we present timing results illustrating how the the evaluation of one time iteration Algorithm 5.1 scales with the particle number N.

Table 2 shows the timing results for $N = \{250, 500, 1000, 2000\}$ particles. The particles lie in a $L_x \times L_y$ computational domain and we use $N_{\text{bdy}} = 70$ boundary points per particle. Their shape, disks with radius a = 1 and decay length $\rho = 4a$, remains the same as previously and their centers and orientations are randomly generated in a way that avoids overlapping boundaries.

The columns include the percentage running time of GMRES (the computationally most intensive step) and total running time that includes the QBX initialization steps. In the tests of Table 2, which starts from random initial data, about two thirds of the simulation time goes into solving for the surface potential σ . (We found that a tolerance $tol_{\rm GMRES}=10^{-5}$ gave sufficiently good numerical accuracy for the purposes of examining the particle dynamics.) In Algorithm 5.1, however, we can use the surface potential σ calculated in the previous time-step as an initial guess for GMRES iterations. This typically reduces the GMRES iterations by a factor of four.

The rightmost column shows the total running time relative to the reference time $T_{\rm ref}=10$ sec. for the 25 particle simulation. The results, which use an 8 core Intel(R) Xeon(R) CPU E5-2650 v4 @ 2.20GHz for hardware, scale linearly with N. On a modern computing cluster, most of the calculations, such as GMRES iterations, source evaluations, symbolic representations, FMM evaluations and numerical integrations, can run in parallel. We therefore expect to have optimal computational cost when running large scale simulations in future studies.

S3. Movie Captions.

Movie S1. Three Particles There are three circular particles with radius 1 centered at $\mathbf{a}_1 = \langle 0, 0 \rangle$, $\mathbf{a}_2 = \langle 2.5, 3.3 \rangle$ and $\mathbf{a}_3 = \langle 2.5, -1.5 \rangle$ and the corresponding orientations θ_1 , θ_2 and θ_3 are 0.1π , $\frac{4}{3}\pi$ and $-\frac{1}{3}\pi$. In this movie, each arrow represents the director of coarse-grained lipid particles where it points from lipid head toward lipid tail. All white dots in the domain represent the tracers in fluid that move with respect to calculated fluid motion. The colored field from dark blue to dark red shows the magnitude of hydrophobic attraction activity and the range is from 0 to 1. Particle 1 and 2 pair quickly aggregate and squeeze the fluid out resulted that the generated fluid flow pushes particle 3 further away from the particle pair. After few frames, due to a non-zero hydrophobic attraction activity between particles, particle 3 rotates and move toward the particle pair to reach the energy minimum. It is clear to see that the fluid is been excluded completely at the last state of the movie. This movies includes a total 100 time steps where the time step is $\Delta = 1.0$.

Movie S2. Twenty-Five Particles There are 25 circular particles with radius 1 initially located on a 5-by-5 matrix grid and the initial orientations θ_i are normally distributed about $\theta=0$. In this movie, each arrow represents the director of coarse-grained lipid particles where it points from lipid head toward lipid tail. All white dots in the domain represent the tracers in fluid that move with respect to calculated fluid motion. The colored field from dark blue to dark red shows the magnitude of hydrophobic attraction activity and the range is from 0 to 1. All 25 particles begin from forming a number of micelle like groups and then assemble to three short bilayers. Here the minimal energy is not completely reached and all endpoints of 3 bilayers move toward non-zero activity field. At final equilibrium state, a vesicle is formed and a energy minimum is achieved. As suggested by HADF, the fluid is separated into two parts, outside and inside of the vesicle. This movies includes a total 800 time steps where the time step is $\Delta t=1.0$.

Movie S3. One Hundred Particles This movie adopts the constant drag law to perform dissipative dynamics. We show the simulation results for 100 particle placed on a 10-by-10 grid with random orientations. In this movie, each arrow represents the director of coarse-grained lipid particles where it points from lipid head toward lipid tail. The colored field from dark blue to dark red shows the magnitude of hydrophobic attraction activity and its range is from 0 to 1. The parameter set is as follows, $\xi_{\mathbf{x}} = 1.5$, $\xi_{\theta} = 2.0$ and $\Delta t = 0.5$. All particles start from forming particle pairs or small groups then these components form micelles and bilayers. In order to reach energy minimum, some groups form long bilayers. Notice that the bilayer on the top-right corner, the transition from an arc to straight shape gives a perfect example for the process of energy minimization. Also, all micelles in the last frame have symmetric shapes. This movies includes a total 1200 time steps.